Building the Noncollinear Optical Parametric Amplifier at the KMC3-XPP beamline of the BESSY II synchrotron

By

ANDRII SHCHERBAKOV

internship report

INSTITUTE OF PHYSICS AND ASTRONOMY OF POTSDAM UNIVERSITY
HELMHOLTZ ZENTRUM BERLIN
FACULTY OF SCIENCES OF LE MANS UNIVERSITY
PHYSICS FACULTY TARAS SHEVCHENKO NATIONAL UNIVERSITY OF KYIV

Supervisor: Prof. Matias BARGHEER
Co-Supervisor: Prof. Brice ARNAUD
Co-Supervisor: Prof. Leonid POPERENKO

ACKNOWLEDGEMENTS

This report is a summary of my work of past 5.5 month in role of an intern student in the group for Ultrafast dynamics of condensed matter (UDKM) at the Institute for Physics and Astronomy of Potsdam University and Helmholtz Zentrum Berlin in Germany in a framework of Master 2 academic mobility program between Le Mans University in France and Taras Shevchenko National University of Kyiv in Ukraine. I want to thank all of these instititions for hosting me and their professors who provided interesting lectures and made great influence on me as on a future scientist.

I would like to express my gratitude to my supervisor Prof. Matias Bargheer, who let me become a member of his group and offered an interesting topic for research. I also want to thank my French and Ukrainian co-supervisors Prof. Brice Arnaud and Prof. Leonid Poperenko for helping with administrative processes and making the valuable comments to my work. I also wish to strongly acknowledge Prof. Thomas Pezeril, without whom I would not participate in the international academic mobility program and who recommended me to the Ultrafast dynamics in condensed matter research group. It is hard to over-evaluate his input.

I want to thank with capital letters Matthias Rössle, who helped me in all aspects of my work, daily life, taught me how to deal with optical staff, and simply was the great interlocutor during the all period of my internship. I studied much from Matthias and it was a pleasure for me to work with him.

I would also like to extend my gratitude to Marc Herzog and Alexander von Rapport for their help, suggestions in planning the experiment, their fair critics and recommendations. I surely want to bring out of shadow Marwan, Jan, Wolfram, Liza, Felix, Max, Stefan, Axel, other members of UDKM group who deeply helped me to get integrated in their research group.

I was always supported by my family and close friends during my work, especially in the moments of emotional weakness, that is why I want to express my grate appreciation to Yuliia Shcherbakova, Olga Shcherbakova, Yuliia Kuznetsova, Olga Gordienko, Olexandr Shcherbakov as members of my family and Danylo Babich, Rostyslav Danylo, Mariia Gryzlova, Andrii Pocherpailo, Nikita Lankin, Roman Rogoza as my friends for 24/7 hours of motivation and support.

In the end I would like to thank my mates from Kyiv and Le Mans, especially Anton Vorobiov, Petro Kovanji, Ruslan Ryskulov and Serhii Derenko for the information support and friend concurrence during our studies.

Abstract

There are several of nonlinear processes which take place in our NOPA: second harmonic generation due to frequency doubling, third harmonic generation due to sum frequency generation, white light supercontinuum generation, and noncolinear optical parametric amplification. The two stage NOPA was designed in accordance with the conditions of restricted place, transportability, and a broad spectral range of output wavelengths. The optimal phase matching angles, noncollinearity angles, and the distances at which the optical elements should be placed for optimum efficiency but without their destruction, were calculated and the consequences explained. The output of the 3ω-NOPA was characterized and pulses with the power up to 17mW in a 475 nm – 700 nm spectral range were measured. The Fourier limit of 3ω-NOPA pulses was also found, therefore their calculated durations are much shorter than 600 fs input beam and vary between 50 fs and 10 fs. In addition, all of the adjustment processes were explained in detail, so it is possible to use this internship report as a guide for the building and adjustment of new NOPAs.

Keywords
Nonlinear optics, noncollinear optical parametric amplification, second harmonic generation, third harmonic generation, supercontinuum generation, BBO, nonlinear crystal.

Table of Contents

Chapter 1

Introduction

There are many processes in the nature that occur on very short time scales. In order to investigate them the detection techniques have at least to be as fast as the processes of interest. For atomic motions during chemical reactions, molecular vibrations, photon absorption and emission etc. the time scale is in the range of fs, phonon dynamics and sound wave propagation takes place on the ps to ns scale, domain wall propagation on a ns to μs scale.

There are many different methods available, which allow to reach different time scales like stopped-flow method (milliseconds) [21], method of flash photolysis (microseconds) [8] or fast photo-diodes and stroboscopic oscilloscopes since 1950 (10^{-10}s) [7, 20]. The best time resolution is available for current Pump-Probe techniques that allow to investigate processes with attosecond time resolution but are routinely used to capture fs dynamics. The Pump-probe method was invented in 1960ies when the appearance of the Q-switching techniques reduced the laser pulse duration by a factor of 10^4 and allowed to generate the nanosecond pulses. The idea of this method is based on the stroboscopic effect when the system is excited and its response is captured after some delay with a "probe". The collection of snapshots at different delays finally allows to reconstruct the transient dynamics of the sample response.

In Figure 1.1 (a.) the classical optical Pump-Probe technique is sketched. An ultrashort laser pulse is generated by a laser. Then it is split by a beamsplitter in two beams: the pump beam and the probe beam. The intensity of the pump beam is always much higher than the probe beam so that the probe does not induce additional dynamics to the sample. The pump beam goes directly to the sample and excite it, usually by thermal heating, generation of free charge carriers, or the generation of ultrafast sound waves. The probe beam is delayed by the delay line before it captures the dynamics of the sample. The optical length of this line is adjustable, so the delay can be varied. Optionally the wavelength of the pump beam can be changed by an optical parametric generator, which allows to excite the sample at different wavelength(s). The scheme on Figure 1.1

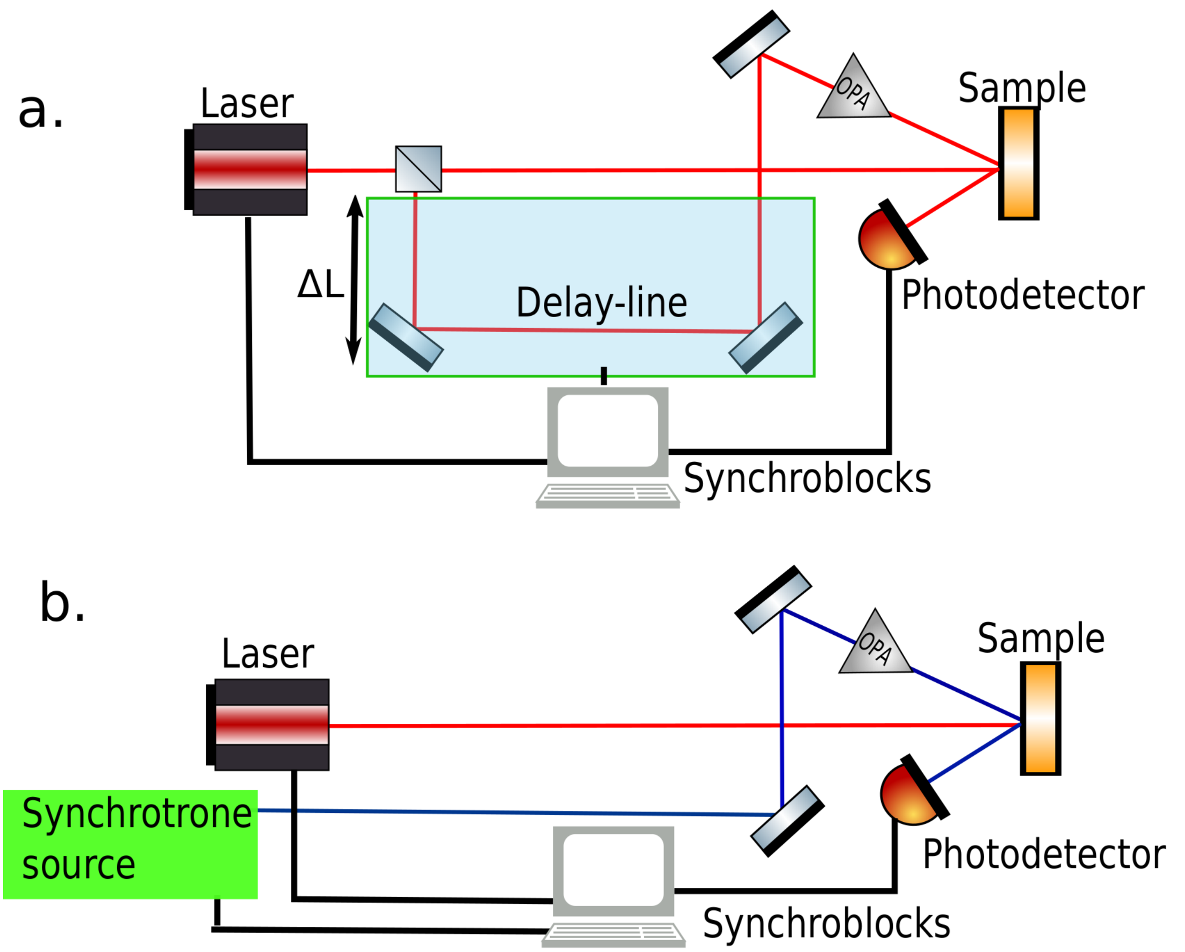

Figure 1.1: The typical scheme of the reflection pump-probe experiment where the laser beam (red line) is used both for excitation of the sample and probing it (a.) and where the laser beam excites the sample but X-Ray synchrotron laser beam probes it (b.).

(a.) shows the case of studying of optical reflection of the sample and the same experiment can be performed in transmission mode. After the reflection, the change of the probe light is captured by a detector. The advantage of this method is that we are not severely limited by the response time of the (photo)detector. We measure the average response and from the repetition rate it is possible to calculate the real reflected signal.

During past few years people developed sophisticated synchronisation techniques, therefore today it is possible to use different sources of electromagnetic waves for pump and probe beams. For example the pump beam can be produced by a laser and the probe beam - by a synchrotron. Using X-rays allows to obtain the direct information about the arrangement of the atoms and distances between them , hence allow to probe the structural response of the sample due to the optical excitation (Figure 1.1 (b.)).

The choice of the pump and probe laser beam wavelength strongly depends on the processes in materials that are investigated and, of course, on the material structure and its properties. The pulse must be sufficiently short, the wavelength must be chosen in accordance with, for example, possible interband and intraband. Typically used amplifier-based laser sources deliver laser pulses with a certain bandwidth, which is not broad enough to resonantly excite the sample a wide range of materials. A solution is the noncolinear optical parametric amplifier ("NOPA"), which can produce electromagnetic waves in the visible and near IR range of wavelength range that differ from the input wavelength of the laser source. Such a NOPA is now set up at the KMC3-XPP BESSY II synchrotron beamline and this process is described in this report. It will be used for the selective excitation of samples for X-ray probe experiments at the KMC3-XPP endstation.

In this work we will first briefly introduce nonlinear optical processes like second harmonic generation, third harmonic generation, white light generation, and noncolinear optical parametric amplification from the theoretical point of view, explain the design considerations for our own NOPA and explain how to adjust it to reach a broad-band amplification of different wavelengths and optimum efficiency.

CHAPTER 2

LITERATURE OVERVIEW

2.1 Basics of Nonlinear optics

Since childhood everyone knowns the wide range of simple optical phenomena based on the processes of refraction, reflection, dispersion, interference, diffraction, etc. These effects are explained by properties of light that do not depend on the light intensity but on its frequency. Maxwell's theory was based on the fact that the light waves do not "feel" each other, i.e., the light wave cannot be scattered at another light wave [16]. The optical effects, which exhibit these properties, are summarized in the field of "LINEAR OPTICS".

After the invention of lasers, people have a light source, of high coherence and high power. It was found that monochromatic light of high intensity can change its colour while propagating in transparent crystals. Also, the phenomenon of self-focusing of intense light in crystals was discovered. These effects proved that light waves can indeed interact either with other light waves or even with themselves, and that the occurrence of these effects depends on the power of the incoming light. These phenomena are discussed in the framework of "NONLINEAR OPTICS".

In this chapter the origin of the terms "Linear-" and "Nonlinear-" will be described. Also, certain nonlinear effects like second and third harmonic generation, white light generation and light amplification will be briefly explained from theoretical and practical points of view, which will be useful for building the noncollinear optical amplifier that will be described in Chapter 3.

2.1.1 Nonlinear polarisation of dielectric materials

The propagation of electromagnetic waves in a transparent dielectric material changes the charge distribution inside of this material. Taking into account the fact that nuclei are much heavier than the surrounding electrons, which form the electronic shells, the deformation of the electronic orbitals is accompanied by a change of the electron charge distribution. In this way, a dipole is created, which is characterized by its dipole moment $\vec{\mu}$. It is important to note here that the electron shell is disordered on a timescale of 10^{-15} seconds, given by the frequency of the electromagnetic wave which is much faster than ionic polarisation (10^{-12} s) or dipole molecular polarisation (10^{-10} s). Thus, for light in the visible range of the electromagnetioc spectrum, only the electronic polarisation has a significant influence [3].

The electric polarisation of the medium, $\vec{P}$, is the average dipole moment per unit volume:

$$\vec{P} = N\vec{\mu} \tag{2.1}$$

where N is the concentration of dipoles in the volume [25]. Assuming that the response of a medium is instantaneous and homogeneous in the material, the induced polarisation $\vec{P}$ depends on the applied electric field $\vec{E}$

$$\vec{P} = \epsilon_0 \hat{\chi} \vec{E} \tag{2.2}$$

or its projections in Cartesian coordinates [3, 25]

$$P_i = \sum_{k=1}^{3} \epsilon_0 \chi_{ik} E_k \tag{2.3}$$

where ϵ_0 is the vacuum permittivity $\epsilon_0 = 8.8542 \cdot 10^{-12}\mathrm{m}^{-3}\mathrm{kg}^{-1}\mathrm{s}^4\mathrm{A}^2$ and χ_{ik} are the elements of the second rank tensor , $\hat{\chi}$, which is called the tensor of dielectric response or susceptibility tensor. In its diagonal form

$$\hat{\chi} = \begin{bmatrix} \chi_{11} & 0 & 0 \\ 0 & \chi_{22} & 0 \\ 0 & 0 & \chi_{33} \end{bmatrix} \tag{2.4}$$

one obtains for isotropic materials $\chi_{11} = \chi_{22} = \chi_{33}$, for uniaxial crystals $\chi_{11} = \chi_{22} \neq \chi_{33}$, and finally for biaxial crystals $\chi_{11} \neq \chi_{22} \neq \chi_{33}$. From Equation (2.2), it follows that the polarisation $\vec{P}$ linearly depends on the electric field $\vec{E}$, which is sufficient to describe all linear optical effects. Nonlinear optical effects hiwever can be described, when $\hat{\chi} = \hat{\chi}(\vec{E})$ is used in Equation (2.3). Expressing the susceptibility as a series with different powers of the field one yields

$$\chi_{ik} = \chi_{ik}^{(1)} + \sum_{j=1}^{3} \chi_{ikj}^{(2)} E_j + \sum_{j=1}^{3} \sum_{m=1}^{3} \chi_{ikjm}^{(3)} E_j E_m + \dots \, . \tag{2.5}$$

After the substitution of Equation (2.5) into Equation (2.3), one obtains:

$$P_i = \sum_{k=1}^{3} \epsilon_0 \chi_{ik}^{(1)} E_i + \sum_{k=1}^{3} \sum_{j=1}^{3} \epsilon_0 \chi_{ikj}^{(2)} E_i E_j + \sum_{k=1}^{3} \sum_{j=1}^{3} \sum_{m=1}^{3} \epsilon_0 \chi_{ikjm}^{(3)} E_i E_j E_m + \dots = P_{i,\mathrm{l}} + P_{i,\mathrm{nl}} \tag{2.6}$$

It is possible to separate the linear part P_{il} and the nonlinear parts of the electron polarisation P_{inl}:

$$P_{i,\mathrm{l}} = \sum_{k=1}^{3} \epsilon_0 \chi_{ik}^{(1)} E_i \tag{2.7}$$

$$P_{i,\mathrm{nl}} = \sum_{k=1}^{3}\sum_{j=1}^{3} \epsilon_0 \chi^{(2)}_{ikj} E_i E_j + \sum_{k=1}^{3}\sum_{j=1}^{3}\sum_{m=1}^{3} \epsilon_0 \chi^{(3)}_{ikjm} E_i E_j E_m + \ldots \tag{2.8}$$

The terms of $\chi^{(n)}$ decrease quickly as the powers of electric field vector is increased. As a result, essentially every material has nonlinear properties, which however, is only observed at high light field intensities. There is a class of so-called nonlinear crystals that exhibit a large nonlinear susceptibility. These are for example BaB_2O_4 (BBO), KH_2PO_4 (KDP), KH_2AsO_4 (KDA), $NH_4H_2PO_4$ (ADP) and more.

A more detailed analysis of nonlinear part of polarisation shows that if electromagnetic waves with the frequencies ω_1 and ω_2 propagate in a nonlinear medium the terms of polarisation P with frequencies $\omega_1+\omega_2$, $\omega_1-\omega_2$, $2\omega_1$, $2\omega_2$, etc. appear and are contained in the output spectrum of the nonlinear crystal. This is schematically shown in (Figure 2.1).

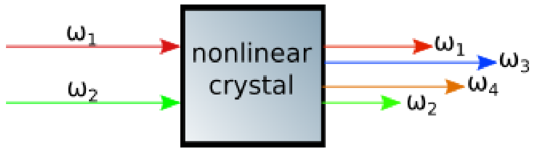

Figure 2.1: Schematic interaction of two waves with different frequencies in nonlinear medium. The new frequencies $\omega_3 =$ and $\omega_4 =$ are generated as indicated by the arrows on the right hand side.

Let us study the general case of interaction of three electromagnetic waves, which we will use in next subsection for the description certain nonlinear effects. It is possible to use quantum optics theory [24] but a classical approach is sufficient for the effects in this thesis [3, 4, 14, 25].

Maxwell's equations for matter [14, 16] are

$$\mathrm{rot}\,\vec{H} = \frac{\delta \vec{D}}{\delta t} + \vec{j} \tag{2.9}$$

$$\mathrm{rot}\,\vec{E} = -\frac{\delta \vec{B}}{\delta t} \tag{2.10}$$

$$\mathrm{div}\,\vec{D} = \rho_{ex} \tag{2.11}$$

$$\mathrm{div}\,\vec{B} = 0 \tag{2.12}$$

where $\vec{D}$ is the displacement field vector, $\vec{B}$ is the vectors of magnetic induction, $\vec{E}$ and $\vec{H}$ are the electrical and magnetic field strength. $\vec{j}$ and ρ_{ex} are the current and charge densities respectively. The mentioned electrical and magnetic values are connected via their constitutive relations

$$\vec{B} = \mu \vec{H} \tag{2.13}$$

$$\vec{D} = \epsilon_0 \vec{E} + \vec{P} = \epsilon \vec{E} \tag{2.14}$$

where the polarisation is determined from Equation (2.7) and Equation (2.8) as

$$\vec{P} = \epsilon_0 \chi^{(1)} \vec{E} + \vec{P}_{\mathrm{nl}}\ . \tag{2.15}$$

In these expressions μ is the magnetic permeability, which in the optical wavelength range is typically equal to the vacuum permeability $\mu_0 = 4\pi \cdot 10^{-7}\mathrm{N{\cdot}m}^{-1}$.

Inserting the electrical constitutive relation into Ampere's law (Equation (2.9)) and after the application of rot-operation of Faraday's law of induction (Equation (2.10)). One obtains the wave equation of light propagation:

$$\nabla^2 \vec{E} = \mu_0 \frac{\delta}{\delta t}(rot\vec{H}) = \mu_0 \sigma \frac{\delta \vec{E}}{\delta t} + \mu_0 \epsilon \frac{\delta^2 \vec{E}}{\delta t^2} + \mu_0 \frac{\delta^2 (\vec{P}_{nl})}{\delta t^2} \quad . \tag{2.16}$$

Here σ means the conductivity and $\epsilon = \epsilon_0 \left(\chi^{(1)} + 1\right)$ is the linear electric permittivity of the media. For the derivation of Equation 2.16, an isotropic medium is assumed, which allowed to use $\operatorname{div} \vec{E} = 0$ [3, 5]. For waves propagating along the z-direction, one obtains the following solutions of the electric field strength:

$$E_i^{\omega_1}(z,t) = \frac{1}{2}\left[E_{1,i}(z)e^{i(\omega_1 t - \kappa_1 z)} + c.c.\right] \tag{2.17}$$

$$E_k^{\omega_2}(z,t) = \frac{1}{2}\left[E_{2,k}(z)e^{i(\omega_2 t - \kappa_2 z)} + c.c.\right] \tag{2.18}$$

$$E_j^{\omega_3}(z,t) = \frac{1}{2}\left[E_{3,j}(z)e^{i(\omega_3 t - \kappa_3 z)} + c.c.\right] \tag{2.19}$$

with the Cartesian coordinates i, j and k of the fields.

In general the field amplitudes depend on the z-coordinate but if the nonlinear polarisation $\vec{P}_{nl} = 0$, the amplitudes will be constant. Historically, the second order susceptibility tensor is always expressed using the tensor $\widehat{d}_{ikj} = \frac{1}{2}\widehat{\chi}_{ikj}$ that does not depend on the frequency ω of the electromagnetic wave [3]. Because of its symmetry properties of the last two indices,which is valid whenever Kleinman's symmetry condition applies [5], it is possible to express $\widehat{d}_{ikj}$ in a form of 3x6 matrix $\hat{d}_{3x6}$, where the following substitutions were made: $xx = 1$; $yy = 2$; $zz = 3$; $yz = zy = 4$; $xz = zx = 5$; $xy = yx = 6$. Therefore, the relation between the components of the nonlinear polarisation of second order and the product of electric field components, for example for frequency doubling, becomes

$$\begin{bmatrix} P_{x,nl} \\ P_{y,nl} \\ P_{z,nl} \end{bmatrix} = \epsilon_0 \begin{bmatrix} d_{11} & d_{12} & d_{13} & d_{14} & d_{15} & d_{16} \\ d_{21} & d_{22} & d_{23} & d_{24} & d_{25} & d_{26} \\ d_{31} & d_{32} & d_{33} & d_{34} & d_{35} & d_{36} \end{bmatrix} \begin{bmatrix} E_x^2 \\ E_y^2 \\ E_z^2 \\ 2E_zE_y \\ 2E_zE_x \\ 2E_xE_y \end{bmatrix} \quad . \tag{2.20}$$

Taking into account that the field amplitudes slowly vary:

$$\frac{\delta E_{1,i}}{\delta z} \gg \frac{\delta E_{1i}^2}{\delta z^2} \tag{2.21}$$

and assuming that the wave vector $\kappa^2 = \omega^2 \mu_r \epsilon_r$ with μ_r and ϵ_r being the relative permittivity and permeability of the medium, respectively one finally gets expressions of the variation of the field amplitude components that depend on two other projections of the electric field vector amplitude:

$$\frac{\delta E_{1i}}{\delta z} = -\frac{i\omega_1 \epsilon_0}{2}\sqrt{\frac{\mu_0}{\epsilon_1}}\, d'_{ijk} E_{3j} E^*_{2k} e^{-i\Delta k z} \tag{2.22}$$

$$\frac{\delta E_{2k}}{\delta z} = -\frac{i\omega_2 \epsilon_0}{2}\sqrt{\frac{\mu_0}{\epsilon_2}}\, d'_{kij} E_{1i} E^*_{3j} e^{i\Delta k z} \tag{2.23}$$

$$\frac{\delta E_{3j}}{\delta z} = -\frac{i\omega_3 \epsilon_0}{2}\sqrt{\frac{\mu_0}{\epsilon_3}}\, d'_{jik} E_{1i} E_{2k} e^{i\Delta k z} \quad . \tag{2.24}$$

Here $\Delta k = \kappa_3 - \kappa_2 - \kappa_1$ is called phase mismatch and the Einstein summation is taken in field vector projection multiplication. The tensor $\hat{d}'$ is derived from $\hat{d}$ after the transformation of the coordinate system.

2.1.2 Dispersion and birefringence

The index of refraction of the transparent materials changes its value depending on different factors. The dependence on the frequency (wavelength) of the electromagnetic wave is called dispersion. An empirical wavelength-dependence that describes a transparent material is for example given by the so-called by Sellmeier's model [17], which covers the spectral range between the inter- and intraband transitions and the phonon region. It is defined as

$$n^2(\lambda) = 1 + \sum_{m=1}^{2} \frac{\lambda^2}{\lambda^2 - \lambda_m^2} A_{\mathrm{disp},m} \quad . \tag{2.25}$$

It should be noted that this approach works only for normal dispersion, that is, $\frac{dn}{d\lambda} < 0$ and do not work properly in the vicinity of resonance line where the imaginary part of the complex refractive index is no longer zero. Using the Sellmeier model given by Equation (2.25) in order to parametrise the refractive index of a BBO crystal, it is possible to write

$$n_o = \sqrt{2.7359 + \frac{0.01878}{\lambda^2 - 0.01822} - 0.01354\lambda^2} \tag{2.26}$$

where λ is given in units of [μm]. In Figure 2.2 the wavelength-dependence of the refractive index for the ordinary and for extraordinary directions of the birefringent BBO is shown.

Nonlinear crystals are often uniaxial crystals that means that the velocity of propagating electromagnetic waves in these crystals depends on their propagation direction and polarisation. Each uniaxial crystal has its the special direction, which is called the axis of this crystal. When the light wave is incident onto the nonlinear crystal surface at an angle θ to the optical axis of the crystal, it splits into two waves with different polarisations and different propagation velocities. The first wave has the field vector $\vec{E}$ that is perpendicular to the plane defined by the optical axis and incident beam . It is called ordinary wave and the propagation velocity does not depend on

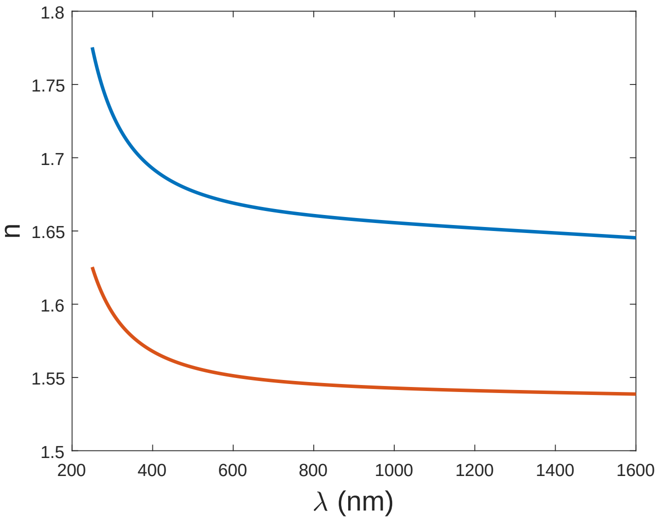

Figure 2.2: The graphical dependence of ordinary index of reflection n_0 (blue curve) and extraordinary index of reflection n_e (orange curve) for BBO crystal.

the direction of propagation. The second wave is polarised in the plane of optical axis and incident beam and is called extraordinary wave. The indices of refraction can be represented by rotational ellipsoids where the axes represent the indices of refraction along the directions parallel and perpendicularly to the crystal optical axis. The length of the radius vector from the center of ellipsoid to the surface yields the refractive index along this direction. For the ordinary wave, of course the ellipsoid becomes a sphere [17] because its velocity is the same along all directions.

There are two types of uniaxial crystals, which are called optically positive and negative. Positive crystals have an extraordinary index of refraction larger or equal to the ordinary one [3] and for negative crystals the opposite situation is the case. There is however always only one refractive index in the direction of the optical axis. Returning to the example BBO, which is a negative uniaxial crystal, that means that its ellipsoid of n_e is smaller than the one for n_o. This is sketched in Figure 2.3. They differ only by a few percent but this will become important for the nonlinear optics, as will be seen in following chapters.

If the axis n_o and n_e of ellipsoid are known, the extraordinary index of refraction as a function of θ can be calculated as follows:

$$n_e(\theta) = \frac{n_o n_e}{\sqrt{n_o^2 \sin^2(\theta) + n_e^2 \cos^2(\theta)}} \ . \tag{2.27}$$

The dispersion conditions are almost the same for the extraordinary index of refraction, just coefficients will be different. For previously mentioned BBO the dispersion relation for the extraordinary refractive index is:

$$n_e = \sqrt{2.3753 + \frac{0.01224}{\lambda^2 - 0.01667} - 0.01516\lambda^2} \ . \tag{2.28}$$

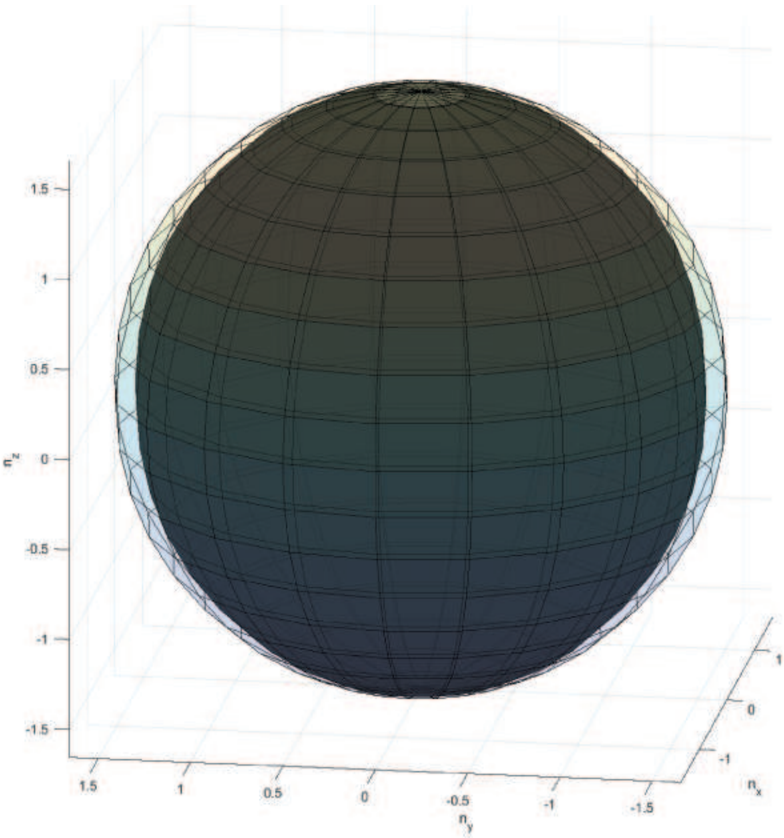

Figure 2.3: Ellipsoids of ordinary index of reflection n_o (outer ellipsoid) extraordinary index of reflection n_e (inner ellipsoid) at 1028 nm of wavelength for BBO crystal.

which is graphically shown in Figure 2.2 by the orange curve.

2.1.3 Second and third harmonic generation

In Sections 2.1.1 and 2.1.2 the basic statements of nonlinear optics were introduced and the coupled equations for field amplitudes (Equations (2.22) to (2.24)) were given. It is now possible to use them to describe the nonlinear effects that will be used in the experimental part of this work and, of course, to obtain some significant expressions, which will allow to optimize the experimental set up and reach high efficiencies of nonlinear optical processes.

To describe the second harmonic generation (SHG) or frequency doubling, which is a special case of sum-frequency mixing. Starting from the expressions for the amplitudes of the incident electromagnetic waves given by Equations (2.22) to (2.24), it is possible to restrict oneself for the case of the angular frequencies $\omega_1 = \omega_2 = \omega$ that will not change as a function of z during generation of the second harmonic: $\frac{\delta E^{(*)}_{1i(2k)}}{\delta z} = 0$. This in turn means that it is possible to consider only of the last Equation (2.24) and assume the amplitude of the SH wave of angular frequency

$\omega_3 = 2\omega$ to be as zero an the entrance surface of the nonlinear crystal: $E_{3j}(0) = 0$. Integrating Equation (2.24) from 0 up to the length L of the nonlinear crystal, one obtains:

$$E_{3j}(z) = -\omega\epsilon_0\sqrt{\frac{\mu_0}{\epsilon_3}}d'_{jik}E_{1i}E_{2k}\frac{e^{i\Delta kL}-1}{\Delta k} \tag{2.29}$$

where the Einstein's summation is used. In general the right hand side of Equation (2.29) contains four terms: xx, xy, yx, yy. If the cross terms xy, yx are much larger then xx and yy, either because of phase synchronism or larger tensor elements. Then the xx, yy terms can be neglected. Because of the symmetry of $\hat{d}'$ an additional factor of 2 appears. Finally the intensity of second harmonic is:

$$I_{\text{SHG}} = \frac{1}{2}\sqrt{\frac{\mu_0}{\epsilon_3}}E_{3j}E^*_{3j} = 8\frac{\omega^2 d'^2_{jik}L^2}{cn_1n_2n_3}I_1I_2\text{sinc}^2\left(\frac{\Delta kL}{2}\right) \tag{2.30}$$

where $c = \frac{1}{\sqrt{\mu_0\epsilon_0}}$ is the speed of light, I_1 and I_2 are the intensities of the incident waves and, n_i are indexes of refraction that are $n_i = \sqrt{\frac{\epsilon_i}{\epsilon_0}}$.

If the incident wave was polarised at 45°, which means that the projections of the intensity on the x and y axes are the same and equal to the half-intensity of incident beam $I_1 = I_2 = I_{\text{in}}$, it is possible to express the efficiency of SHG relative to the intensity of the incident wave:

$$\eta_{\text{SHG}} = \frac{I_{SHG}}{I_{\text{in}}} = 2\frac{\omega^2 d'^2_{jik}L^2}{cn_1n_2n_3}I_{\text{in}}\text{sinc}^2\left(\frac{\Delta kL}{2}\right) . \tag{2.31}$$

The same is result is obtained if one uses the xx and yy components [3]. The factor of 2 in Equation (2.31) might be missing in some literature sources because of the determination of the complex field amplitudes. It is important to remember that this approach works only when the SHG light intensity is much smaller than the intensity of the incident light, otherwise the law of energy conservation would be violated.

The third harmonic can be generated in different ways. Mostly, when people talk about it, the third order effect is meant when the cubic nonlinear susceptibility tensor $\hat{\chi}^{(3)}$, which is rank-4 tensor, plays a dominant role. But this requires either much higher intensities of the incident beam or finding a new nonlinear crystal where the components of described tensor will be sufficiently large. Another way to produce frequency-tripled light to first frequency-double it ($\omega \to 2\omega$) and then do the sum-frequency mixing of the doubled frequency light and incident single frequency so that $\omega + 2\omega \to \omega_3 = 3\omega$ [3, 13, 22]. This approach will also be used for the UV pumped mixing stage of the set up NOPA. Without detailed explanation it is possible to follow the same idea than for SHG light and write down the expression for the intensity of the sum frequency generated (SFG) light as

$$I_{\text{SFG}} = 2\frac{(3\omega)^2 d'^2_{jik}L^2}{cn_\omega n_{2\omega}n_{3\omega}}I_\omega I_{2\omega}\text{sinc}^2\left(\frac{\Delta kL}{2}\right) . \tag{2.32}$$

Studying the expressions for the intensity of the generated light given by Equations (2.30) and (2.32), one sees a periodical dependence in form of a sinc^2 function, which is shown in

Figure 2.4. In the minima of this function its argument is equal to

$$\frac{\Delta k L}{2} = n\pi \tag{2.33}$$

where n is an integer and $n \neq 0$. From this one may conclude that during the propagation of the fundamental light new frequencies are generated at the beginning, however, after some time the energy will be transferred back to the fundamental wave.

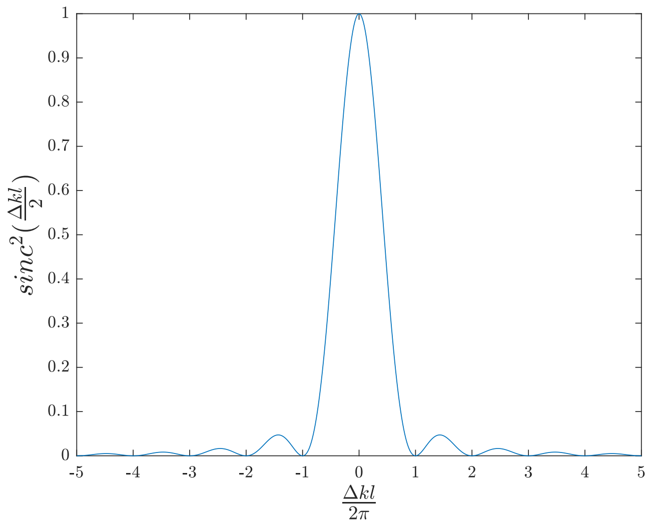

Figure 2.4: The graphical dependence of sinc^2 function on its argument

This behaviour suggests the introduction of a new parameter, the so-called coherence length L_{coh}. This is a measure for the propagation length in a nonlinear crystal after which the intensity of SHG or SFG light is still increasing [3]. Thus, the nonlinear crystal does not need to be longer than L_{coh}. This value can be defined from the half of the distance between the zeros of 1^{st} and -1^{st} order

$$L_{\text{coh}} = \frac{\pi}{\Delta k} \ . \tag{2.34}$$

Because the intensity of the generated higher harmonic light is proportional to L_{coh}^2 (see Equations (2.30) and (2.32)), it is important to increase L_{coh}. For the perfect case one obtains $L_{\text{coh}} \to +\infty$ for:

$$\Delta k = 0 \tag{2.35}$$

The case of Equation (2.35) is called "condition of perfect phase matching" [5] or "The condition of phase synchronism" [3]. In reality L_{coh} is of course finite and its value depends on thermally induced scattering losses.

In the following, it is explained how the condition imposed by Equation (2.35) is experimentally realised. Typically, the birefringence of the nonlinear crystals, which was described in

	Positive uniaxial crystal	Negative uniaxial crystal
Type 1	e+e→o	o+o→e
Type 2	e+o→o	o+e→e

Table 2.1: Types of phase matching

Section 2.1.2, is used. For SHG and SFG there are several different wave polarisation configurations for phase matching exist, which are summarised in Table 2.1.

Now the case of Type 1 phase matching for SHG in a BBO crystal, which is an optically negative crystal, is discussed. From Table 2.1 one can see that, two fundamental ω-waves with ordinary polarisation (or just one powerful ω-wave) can generate an e-polarised 2ω-wave. The corresponding phase matching condition is

$$\Delta k = \kappa_{3,e}(\theta) - \kappa_{1,o} - \kappa_{1,o} = \frac{2\omega \cdot n_{3,e}}{c} - \frac{\omega \cdot n_{1,o}}{c} - \frac{\omega \cdot n_{1,o}}{c} = 0 \tag{2.36}$$

that finally leads to

$$n_{3,e}(\theta) = n_{1,o} \ . \tag{2.37}$$

This means that for the highly efficient generation of SHG light it is necessary to determine the phase matching angle using Equation (2.27) and to orient the BBO such that the angle between the optical axis of the crystal and the direction of the e-polarised 2ω light propagation is equal to the phase matching angle angle.

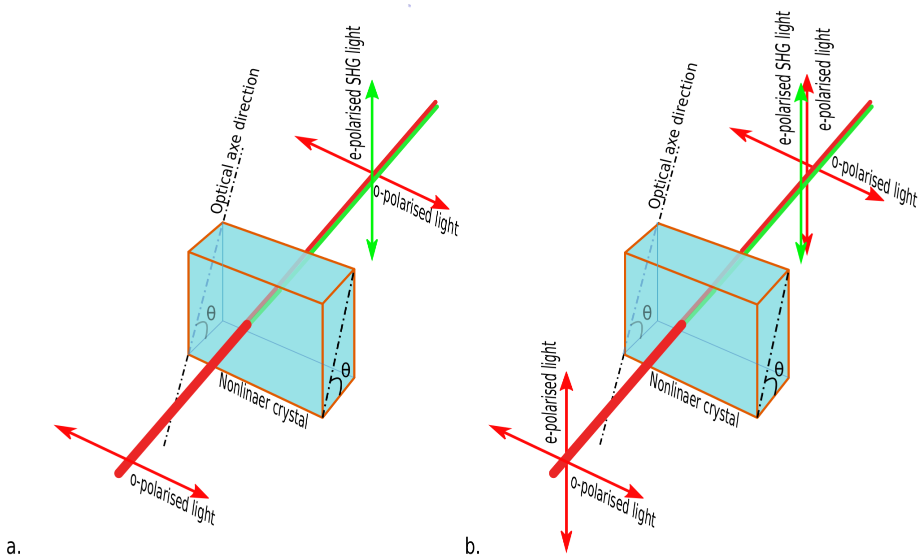

Figure 2.5: The schematic description of Type I (a.) and Type II (b.) configurations of SGH for negative crystal

A similar expression can be obtained for Type 2 SHG phase matching, which yields

$$\Delta k = \kappa_{3,e}(\theta) - \kappa_{1,e}(\theta) - \kappa_{1,o} = \frac{2\omega \cdot n_{3,e}(\theta)}{c} - \frac{\omega \cdot n_{1,e}(\theta)}{c} - \frac{\omega \cdot n_{1,o}}{c} = 0 \ . \tag{2.38}$$

$$n_{3,e}(\theta) = \frac{n_{1,e}(\theta) + n_{1,o}}{2} \tag{2.39}$$

Here Equation (2.27) has to be substituted twice for $n_{3,e}(\theta)$ and $n_{1,e}(\theta)$.

2.1.4 White light generation

The white light generation (WLG) or the supercontinuum generation is a frequently used phenomenon in the field of nonlinear optics. WLG is actively investigated [6, 9] because of the wide range of different optical spectral ranges obtained depending the generation parameters like laser wavelength, laser fluence, pulse length, and material used for the WLG. The generated white light spectrum is preferentially directed along the propagation direction of the incoming light waves, highly coherent, and it is possible to generate ultrashort white light pulses with a polarisation determined by the polarisation of the incoming laser pulse [6, 9].

The three main regimes of WLG are known as soliton fission regime, Modulation instability regime, and pumping in the normal dispersion regime. The first two modes are applicable mostly for fibres [13]. For the setup of the NOPA the last mode is important: WLG will be performed in a transparent medium with normal dispersion and in the following, this is discussed.

To date the most common explanation of WLG is based on the nonlinear effects: self-focusing, self-modulation, and multi-photon absorption/emission with the free electron plasma generation causing the laser beam filamentation [6, 9, 11].

When femtosecond laser pulse is focused in transparent dielectric media, index of refraction n of the medium depends due to the third order nonlinearity on the light intensity I is given by:

$$n = n_0 + n_2 I \tag{2.40}$$

where n_2 is the nonlinear refractive index. Because of the Gaussian beam profile of the laser beam (see Section 2.2), the laser beam becomes self-focussed due to the Kerr-lens effect in the nonlinear regime of the medium []. When the power of the beam is equal to its critical power for self-focusing, P_{cr}, which is given by:

$$P_{cr} = \frac{3.72\lambda^2}{8\pi n_0 n_2} \tag{2.41}$$

where λ is the incomming laser wavelength. The diffraction of the light beam in the medium that leads to the beam divergence is compensated by the self-focussing.

Of course, the diminishing beam spot leads to time-dependence of the intensity $I(t)$, that creates an additional phase change of the electromagnetic wave:

$$\phi_{nl}(t) = -\frac{\omega_0 n_2}{c} I(t) \tag{2.42}$$

that finally leads to a change of the circular frequency of the EM wave:

$$\delta\omega = \frac{\delta\phi_{nl}(t)}{\delta t} \ . \tag{2.43}$$

In other words light with the frequencies .

$$\omega = \omega_0 + \frac{\delta\phi_{nl}(t)}{\delta t} \tag{2.44}$$

is generated. Depending on the propagation time and the intensity profile of the laser beam the correction in Equation (2.43) can become either positive or negative and hence lead to a red or a blue shift of the fundamental wavelength [6, 9].

The process of self-focus cannot continue forever. At some point the intensity will be large enough to initiate multi-photon absorption process in generation medium and the material bulk is ionised and a bulk plasma appears. The incoming and generated photons are absorbed, which means that the intensity cannot increase further. This is the reason for the strong dependence of the generated white light sprectrum on the bandgap of the material used for WLG. [9, 11].

2.1.5 Noncollinear optical parametric amplification

The optical parametric amplification is a nonlinear effect based on difference frequency generation [5] that is caused by the second order susceptibility $\chi^{(2)}$.

For this process two waves have to interact: the powerful pump EM wave with angular frequency ω_3, the so-called "pump" beam, and the second EM wave with angular frequency ω_1, the so-called "signal" wave. While both waves propagate in a nonlinear medium, the ω_3 pump photons can split into the ω_1 signal photon and the so-called $\omega_2 = \omega_3 - \omega_1$ idler photon. As an result a wave with the new frequency ω_2 is generated and the mutual amplification ofsignal and idler waves happens.

Starting from the coupled amplitude relations Equations (2.22) to (2.24) one observes a case where the pump beam does not loose its energy, $\frac{\delta E_{3j}}{\delta z} = 0$ Omitting the tensor character of the coupled relations, after some mathematical operations one can write:

$$\frac{\delta^2 E_2}{\delta z^2} = m^2 E_2 \tag{2.45}$$

where m is the coupling factor between the idler and the signal waves, that is given by:

$$m^2 = \frac{\omega_1 \omega_2 d^2 \mu_0}{\sqrt{\epsilon_1 \epsilon_2}} |E_3|^2 \ . \tag{2.46}$$

With the boundary conditions

$$E_1(0) = \text{any} \tag{2.47}$$

and

$$E_2(0) = 0 \ . \tag{2.48}$$

the evolution of the idler and the signal wave amplitudes is [5]

$$E_1(z) = E_1(0)\cosh(mz) \tag{2.49}$$

$$E_2(z) = i\left(\frac{n_1\omega_2}{n_2\omega_1}\right)^{1/2}\frac{E_3}{|E_3|}E_1^*(0)\sinh(mz)\ . \tag{2.50}$$

This spatial dependence is shown in Figure 2.6. The modulus of the field strength for signal and idler EM waves exponentially depend on the propagation distance z and tend to the same value after some propagation. It is important to note that the idler wave depends on the phases of the pump and the signal wave whereas the signal wave depends only on its initial phase [3, 5]. Both waves lead to the decay of the pump photons ω_3: The generation of the idler photons with ω_2 results in a stimulated generation of the signal photons ω_1 and vice-versa.

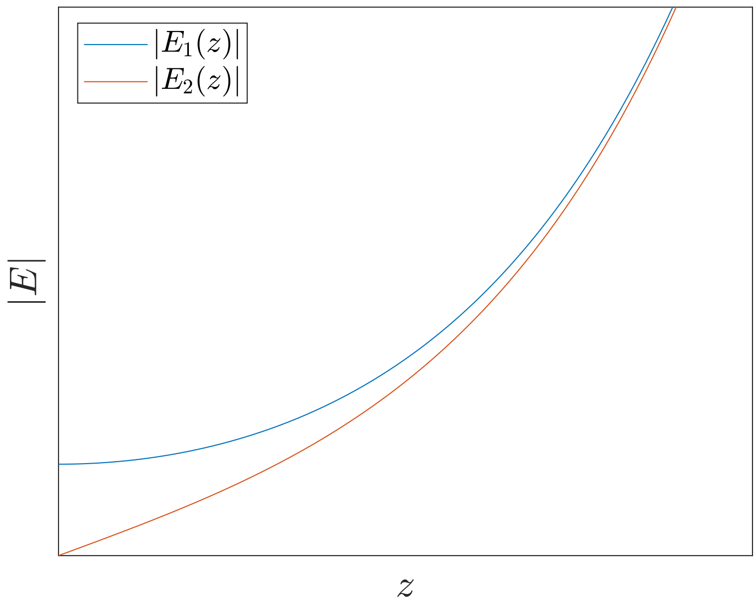

Figure 2.6: The graphical dependence of the modulus of signal wave amplitude $|E_1|$ (blue curve) and idler wave amplitude $|E_2|$ (red curve).

Up to now, the previous expressions were investigated for the perfect phase matching condition given by Equation (2.35). However in a birefringent medium only the phase velocities of the different waves can be matched, not their group velocities. This means that the wave packets of three light waves propagate with different velocities, which leads to a temporal elongation of the signal and idler waves or even stops the amplification [13, 19].This means that the amplification strongly depends on temporal and spatial overlap of the different waves. For the amplification of different wavelengths, this overlap has often to be optimized for the optimum optical conversion and amplification.

In 1995 Gale [10] solved this problem and proposed alternative optical scheme where the three waves propagate not collinearly. For the noncollinear case the phase matching condition acquires the vectorial character

$$\delta\vec{k} = \vec{\kappa}_3 - \vec{\kappa}_2 - \vec{\kappa}_1\ . \tag{2.51}$$

In addition, the energy conservation has to be fulfilled:

$$\omega_3 = \omega_1 + \omega_2 \ . \tag{2.52}$$

In Figure 2.7 the noncollinear configuration is sketched for the wavevectors of pump, signal, and idler waves. Bearing this picture in mind, it is possible to find a scalar relation between the tree wavevectors

$$k_p = k_s \cos(\phi) + \sqrt{k_i^2 - k_s^2 \sin^2(\phi)} \ . \tag{2.53}$$

Here k_p,k_s,k_i are the absolute values of the pump, signal and idler wavevectors, respectively. Also in this configuration the values of the wavevectors depend on the frequency of the different waves as well as on the index of refraction of the generation medium. At the same time the index of refraction in a uniaxial medium for ach wave depends on its polarisation, its wavelength, and its propagation direction. Thus, it is possible to calculate the matching angles ϕ for different wavelengths using the Sellmeier parametrisation of the refractive index given in Section 2.1.2 and the index of refraction ellipsoid given by Equation (2.27).

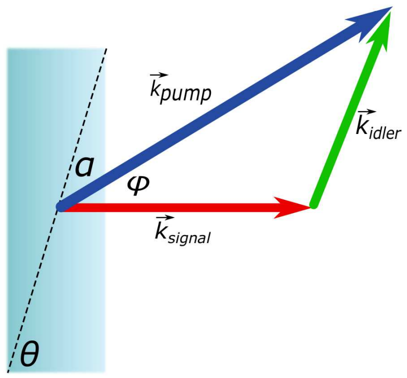

Figure 2.7: Vector diagram for the noncollinear optical parametric amplification scheme in a nonlinear crystal, where θ is an angle between optical axis of the crystal and its short side, ϕ is the phase matching angle and λ is the angle between the pump wave and optical axis.

2.2 Gaussian beams

As it was mentioned in previous sections, one of the required conditions of obtaining high efficiency of nonlinear wave interaction is the usage of light, which has a high intensity and high coherence. The typical sources for producing light with high coherence and intensity are femtosecond lasers. Their pulsed beams have properties that cannot be described anymore in terms of simple geometrical optics and that are important for the generation of the nonlinear optical effects discussed in Sections 2.1.1 to 2.1.5.

It is known from the Maxwell's equations that the wave equation for propagating EM waves in transparent dielectric material is [18]

$$\left[\nabla^2 - \left(\frac{n}{c}\right)^2 \frac{\delta^2}{\delta t^2}\right] \vec{E}(\vec{r},t) = 0 \tag{2.54}$$

with the electric field vector $\vec{E}(\vec{r},t)$, which in general depends on time t and the coordinate r. n is the index of refraction of the transparent medium and c is speed of light in vacuum. This equation can be simplified taking in to account that $\vec{E}(\vec{r},t) = \vec{E}(\vec{r})\mathrm{Re}\left[e^{-i\omega t}\right]$. One finally comes to the Helmholtz wave equation that only depends on spatial coordinates:

$$\left[\nabla^2 - \vec{k}^2\right] \vec{E}(\vec{r}) = 0 \ . \tag{2.55}$$

The wave vector k is defined as $k = \frac{\omega n}{c}$ with the angular frequency ω of the wave. This equation has different solutions but for the discussion in this thesis two in the following solutions are particularly important. The first solution describes plane waves with constant wave vector and field amplitude ξ_0, which is

$$E(\vec{r},t) = \mathrm{Re}\left[\xi_0 e^{-i\omega t - \vec{k}\vec{r}}\right] \ . \tag{2.56}$$

and the second solution describes spherical waves, where the electric field strength and wavevector depend on the radial coordinate r, which is given by

$$E(\vec{r},t) = \mathrm{Re}\left[\xi_0 \frac{e^{-i\omega t - \vec{k}\vec{r}}}{|\vec{k}\vec{r}|}\right] \ . \tag{2.57}$$

It is important to realize that the laser beams of femtosecond lasers have properties that depend on the spatial coordinate, thus consist of properties of planar waves and spherical waves. In Figure 2.8 the change of the EM wavefront is shown as function of the propagation coordinate z after focussing the laser beam with a convex lens. Femtosecond laser pulses are characterised by a Gaussian intensity distribution across their beam cross section far away from the focus and in the focus (in Figure 2.8 at $z = 0$) of this beam, the so-called beam waist with the minimum cross section with diameter w_0 occurs. In the region $2z_{\mathrm{R}}$ of such a so-called Gaussian beam a constant field amplitude along the propagation direction appears.

It is possible to express the intensity profile that contains planar and spherical beam properties dependent on the propagation coordinate. After the extension of the real propagation coordinate z by the complex coordinate $-iz_0$ and one replaces $z \to z - iz_0$. z_0 is a real number that measures the distance to the separate regimes where the beam has spherical properties, that is, where $|z| > z_0$, and regions where plane wave properties dominate, which is the case for $|z| < z_0$ [17, 18]. The resulting wave equation resembles the principal TEM_{00} laser mode [18]. Taking into account the Gouy phase $\eta(z) = \tan^{-1}(z/z_{\mathrm{R}})$ due to the curvature of the planar wave [18], the spatial distribution of the electric field becomes

$$E(\rho,z) = \xi_0 \frac{w_0}{w(z)} e^{[\rho/w(z)]^2} e^{ik\rho^2/2R(z)} e^{i[kz - \tan^{-1}(z/z_{\mathrm{R}})]^2} \tag{2.58}$$

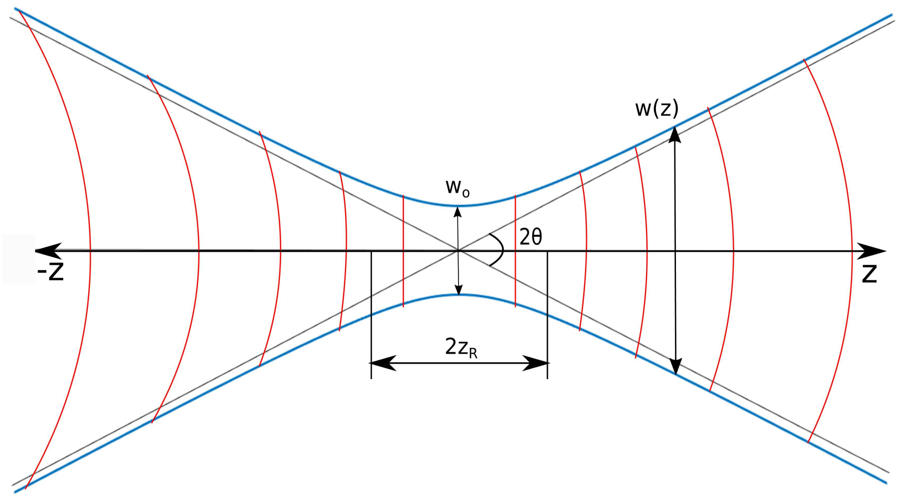

Figure 2.8: The profile of Gaussian beam (blue line) in propagation direction z; Front of Gaussian beam (red line). w_o is the beam waist, $w(z)$ - beam diameter, R_r-Reyleigh range

Respectively the intensity is

$$I(\rho,z) = \frac{c\epsilon_0}{2}EE^* = \frac{c\epsilon_0}{2}|\xi_0|^2\left(\frac{w_0}{w(z)}\right)^2 e^{-2[\rho/w(z)]^2} \quad . \tag{2.59}$$

In Equation (2.58) z_R is the previously described parameter of Lorentzian intensity distribution in z-axis (Figure 2.9(b)) so-called Rayleigh range [23] where $w(z) = w_0\sqrt{(1+(z/z_\mathrm{R})^2)}$ is the beam radius as function of z_R that depends on the distance z to the beam waist with $w_0{}^2 = \lambda z_\mathrm{R}/\pi$ for a laser beam with wavelength λ. The intensity has a Gaussian profile in the plane perpendicular to the propagation direction. Other basic Gaussian beam parameters are the radius of the curvature of the wave front at position z, $R(z)$, and the half opening angle of the divergence, θ_FF which are given by

$$R(z) = z[1+(z_\mathrm{R}/z)^2] \tag{2.60}$$

$$\theta_\mathrm{FF} = \lambda/\pi w_0 \tag{2.61}$$

In Figure 2.8 these quantities are shown for the cross-section of a Gaussian beam. A 3-dimensional representation of the normalised intensity is shown in Figure 2.9a). A cut through the intensity distribution of Figure 2.8 a) at the beam focus position where w_0 is minimum is shown in Figure 2.8 b) and the cut at $z = 0$, that is, along the propagation direction z is shown in Figure 2.8 c). From this one can conclude that strongly focused beam beam has a the smaller waist w_0 and a smaller Rayleigh range z_R but an increased intensity I. In practice, the waist of the laser does not necessarily be located at the laser output. The laser documentation usually contains the information about its size and position and/or graphs of radius variation on the distance to the laser.

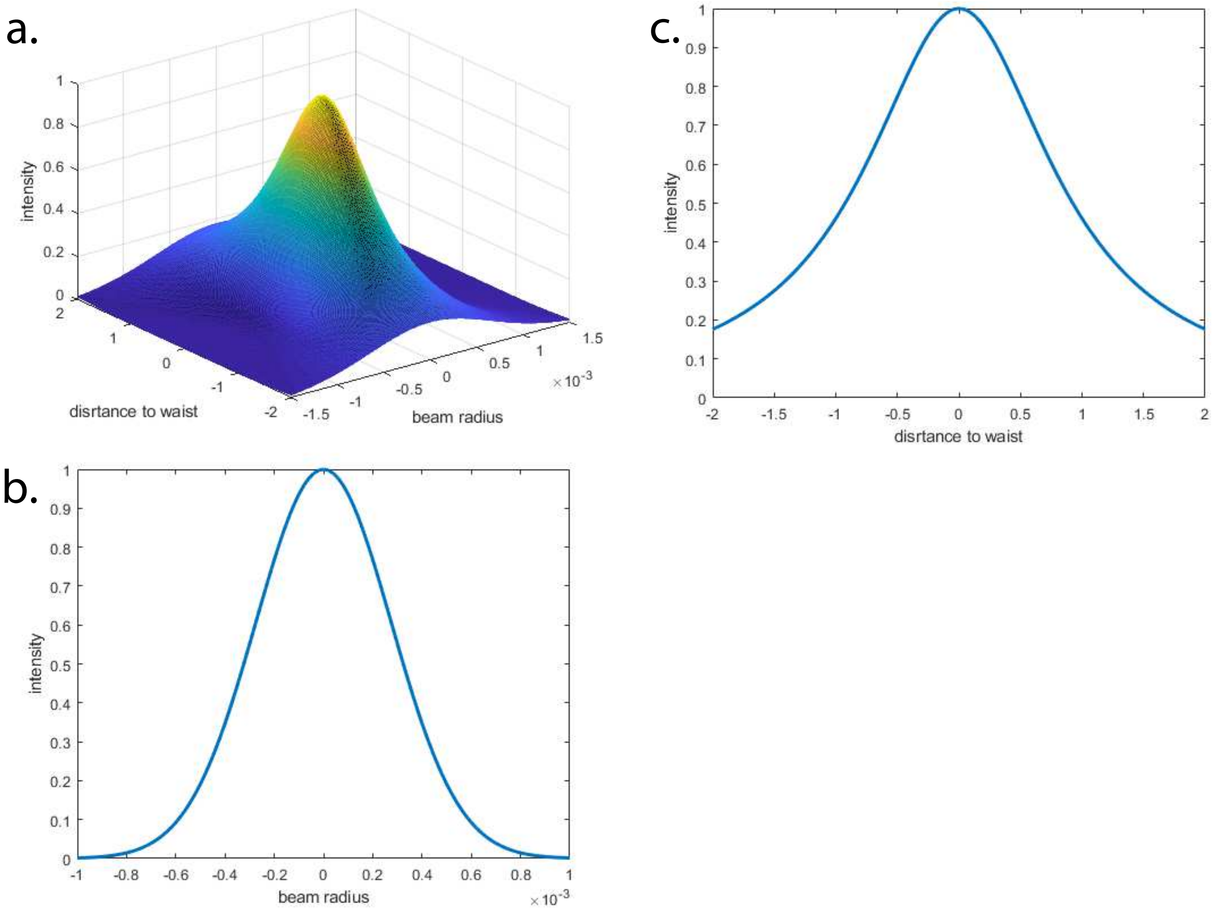

Figure 2.9: The normalized intensity profiles of a Gaussian beam in dependance on the: a. distance to waist and beam radius in meters (3D plot); b. beam radius in meters in the waist (2D plot); c. distance to waist in meters in the center of Gaussian beam (2D plot). The values for waist and wavelength were taken as 1028 nm and 0.55 mm respectively.

The properties of Gaussian beams become particularly important while working with long laser beam paths and using focusing optics. The image creation of a simple convex lenses is described with the well known thin lens equation

$$\pm\frac{1}{d} \pm \frac{1}{f} = \frac{1}{F} \tag{2.62}$$

where d is the distance between the lens and the object, f represents the distance between the lens and the image and F is the lens focal distance. The choice of the signs depends on the reality of the image or of the object. For simplicity let us consider pluses where the object and the image are real.

Siegman recommends to use the universal way to calculate how a Gaussian beam passes through an optical system using the matrix formalism, but for the particular case for a thin

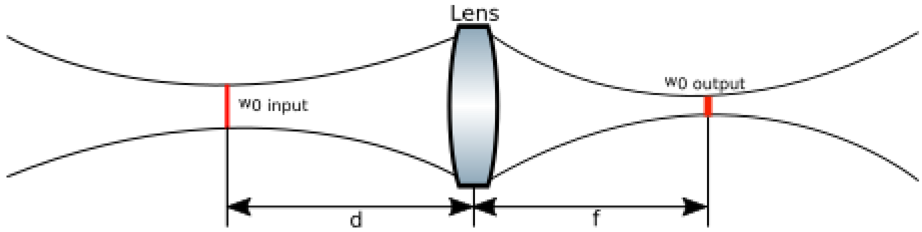

Figure 2.10: A Gaussian beam passing through a convex lens: The beam waist of the incoming laser beam is positioned in the object distance of the lens, d, and the image of the beam waist is observed after the focus distance f of the lens.

convex lens we can use the Gaussian extension of Equation (2.62) [23]:

$$\frac{1}{d + {z_R}^2/(d-F)} + \frac{1}{f} = \frac{1}{F} \ . \tag{2.63}$$

Here the object distance d is assumed to be equal to the the distance to the input waist as shown in Figure 2.10 and one obtains the new waist on the image side of the lens at the distance f. In contrast to the classical geometrical optics, Gaussian optics yield in the case of absent diffraction that the image plane is at infinity if the source is placed in the focus plane. Also the image of a Gaussian beam waist placed in the object distance is imaged in the image distance as shown in Figure 2.10.

Chapter 3

Experimental realisation

In this chapter we review and explain the experimental besics of a building NOPA. We first derive the distances between the optical elements from a simple simulation, then explain the principal NOPA scheme, explain the processes of adjustments, and finally discuss the measured results of the characterization of the built NOPA.

3.1 NOPA design

In this subsection the optical scheme for the noncolinear optical parametric amplifier will be discussed on the basis of the theoretical considerations presented in Chapter 2.

One main point of the NOPA scheme design was put on its compactness because the space at the BESSY II KMC3-XPP beamline is restricted and it should be possible to transfer the NOPA to different experiments. At the same time we are not aiming at the shortest possible NOPA pulse output because the X-Ray pulse duration at BESSY II is between 15 and 70 ps [12] in low-alpha respectively in the more common hybride mode does not require ultrashort pump pulses. We of course try to reduce the pulse duration of the incoming laser pulses from FWHM ~600 fs in order to be able to drive nonlinear optical excitation processes like coherent Raman excitation of phonons or two-photon-absorption across the bandgap of insulators. The main focus of building the NOPA is to obtain powerful pulses that can be turned over a broad spectral range. This NOPA was designed to use two amplification branches where in branch the doubled and in the other one the tripled frequencies of the fundamental wavelength of the laser are used as pump waves.

3.1.1 General characteristics

The general idea of "two branch" NOPA design was taken from [13] and adapted for our needs and prerequisites. The principal scheme of the 2ω-NOPA + 3ω-NOPA is shown in Figure 3.1. It is consists of:

- 1x Pharos Yb (260 fs, 400 μJ, 1028 nm) Laser source
- 1x Breadboard
- 4x Apertures
- Periscope
- Beamsampler
- 11x Different broad spectral range mirrors
- 1x 1/6 Beamsplitter
- 4x Different BBO nonlinear crystals
- 1x Broad spectral range beamsplitter
- 7x Different convex lenses
- 1x Dichroic mirror (reflects 514 nm of wavelength)
- 1x Dichroic mirror (reflects 343 nm of wavelength)
- 1x Sapphire window (4 mm of length)
- 1x Gray filter
- 1x Shortpass filter
- 2x Different spherical mirrors
- 6x Moveable stages

We use a Light Conversion Pharos amplifier. It its typically operated at a repetition rate of 104 kHz, which is the 16th subharmonic of the fundamental BESSY operational frequency of 1.25 MHz. This is important because for the time-resolved laser pump – X-ray probe experiments, the arrival time of the X-ray pulses is fixed and the relative arrival time of the laser pump pulses has to be varied. Therefore the oscillator of the Pharos is synchronized to ring clock using a Menlo RRE Sync synchronization device that acts on the cavity length of the oscillator and together with an electronic delay box (Menlo DDS120), the delay between X-ray pulses and laser pulses

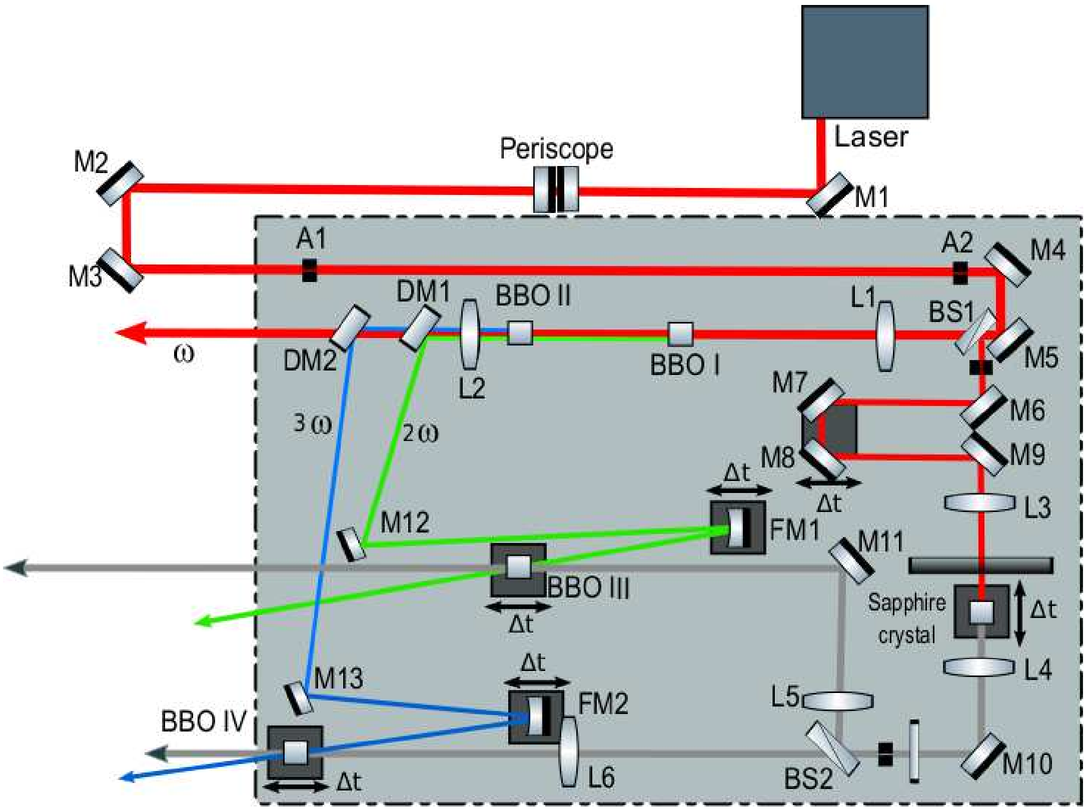

Figure 3.1: General 2ω-NOPA + 3ω-NOPA design.

can be varied remotely. Generally, the Pharos features 600 fs long pulses with 200 μJ of pulse energy. The output wavelength is 1028 nm with an average power of maximum 20 W. However, to be able to vary a little bit the efficiency of the NOPA especially after some time of operation, we opted for an optimized design for the average pump power of 15 W, which of course slightly reduces the available pulse energy but allows us without a complete rebuilt of the NOPA to react on fluctuations and at least for some time compensate the possible degradation of optical components. To allow the usage of the NOPA at different locations we set it up on a 60 cm x 90 x 6 cm optical honeycomb breadboard (Thorlabs B6090A).

The fundamental alignment of the optical components was performed with the reduced average laser power of 150 mW in order to reduce accidental back reflections during the placement of the optical elements on the table. Now we describe the optical beam path from the laser to the NOPA input and explain the beam path in the NOPA in detail. First we use a periscope to lift the laser output beam to the desired beam height of 14 cm on the optical table. Then the still p-polarized laser beam is fed into the NOPA. The beam height of the NOPA elements is fixed to

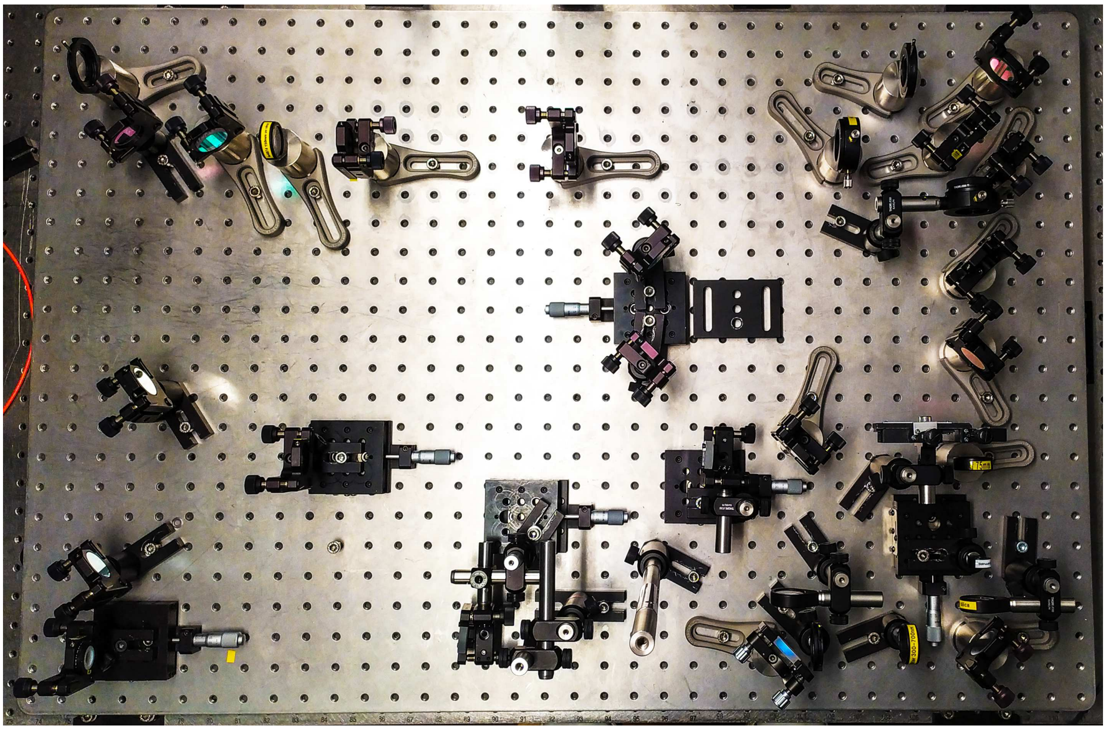

Figure 3.2: The photo of 2ω-NOPA + 3ω-NOPA scheme.

8 cm and we have produced at the workshop of the University of Potsdam posts with the height of XX cm that are clampled to the bread board with Thorlabs clamping forks and fix the reference beam height. Then the incoming light is passed trough the two fixed alignment apertures A1 and A2, that allow to quickly check the incomming beam alignment and thus allows a quick alignment of the NOPA in case it is transportated to a different location. Then the beam is split into a two beams by the 1/6 beamsplitter BS1. The directly passed-through beam with the power of 12,4 W is used to pump the second and third harmonic generation part will be described in the paragraph below and the reflected beam with roughly 2,1 W is used to generate a white light supercontinuum as will be described in Section 3.2.3.

3.1.1.1 Generation of the NOPA pump beams

The pump beams of the subsequent NOPA stages are generated using the optical scheme proposed by Riedle *et al.* [13, 22]: the SH generation of the Type 1 , which theoretical basis was explained in Section 2.1.3, takes place in a 0.8 mm thick BBO crystal (BBO I), which is placed 9cm before the focus of a B-coated focussing lens (Thorlabs) with $f = 300$ mm (L1). The Type II generation of s-polarized TH is done due to the process explained in Section 2.1.4 in the second 5 mm thick BBO II, which is placed 9 cm after the focus of L1. This SHG process is possible because the pulse of the second harmonic propages in the BBO II faster than the fundamental of the laser because of the different signs of the respective group velocities [13] and thus yields the temporal overlap of the pulses for the mixing process. Another 150 mm UV-silica focusing lens (L2) collimates all three beams again. The separation of fundamental, SH and TH light is carried out by two dichroic mirrors, which reflect only the SH (DM1) or the TH (DM2) and are transparent for the other wavelengths. The two pump beams are then subsequently routed towards the focussing mirrors by an additional mirror (Thorlabs E01 for the TH and Thorlabs E02 for the SH), which allows to preadjust the beam path lengths roughly with respect to the white light pulses whose generation is described in the following.

3.1.1.2 White light supercontinuum generation

The supercontinuum generation part starts with the aperture A3, that is used to shape the "tails" of the Gaussian intensity profile. A small delay delay stage allows fine tuning of the delay between SH/TH beams and the white light pulses. Then the light is focussed with a 35 mm fused silica lens (L3) into a 4 mm thick sapphire crystal (a Thorlabs window). For the adjustment of the white light generation condition, the input beam can be attenuated right after the lens by a continuous grey filter (Thorlabs NDL-25C-4) and the focus within the sapphire crystal is shifted towards the end of the crystal by moving it with a small translation stage to the position where the spectrum (see Figure 3.9) is optimum and the stability of the generated white light is good. After that, the white light is collimated by the convergent lens L4 with $f = 25$ mm and – if neccessary – the transmitted fundamental is filtered by a short pass filter with a transmission range between 350 and 700 nm, however, we found that the used beam splitter that equally distributes the WL spectrum to the two NOPA branches already absorbs a significant part of the laser fundamental wavelength. Hence, we usually do not used this filter. The aperture A4 can be used to cut unwanted parts of the generated white light spectrum.

3.1.1.3 The NOPA stages

The noncolinear parametric optical amplification happens in BBO III using the SH pump beam and in BBO IV using the TH pump beam. The 2ω and 3ω pump beams are focused by the 250 mm focusing mirrors FM1 (dielectric Thorlabs E02 mirror) and FM2 (Thorlabs CM254-250-F01, an UV enhanced metallic mirror). The focussing mirrors for the pump beams are placed right below the white light beam axis. With the help of the two prior placed plane mirrors together with the focussing mirrors, the pump beams are directed under the optimum phase matching angles ϕ for broad band amplification as calculated from Equation (2.53). The focusing mirrors are placed on linear stages to adjust the time delay between pump and WL beams in the BBO crystals. The BBO crystals are also placed on linear stages to calibrate the spot size and the intensity of the respective pump beams. As a result, a certain wavelength of the white light spectrum is amplified in dependence on the angle of the incidence of the pump beams into the BBOs and the time delay between the white light and respective pump beam.

3.1.2 Defining the positions of the optical elements

In Chapter 2 we showed that the intensity and the efficiency of generated SH or TH light depends on the multiplication of the intensity of the incident light waves. However, the increase of the intensity leads to self-focusing nonlinear effects in the material with additional white light generation, that is not wanted in this case. At the same time the damage threshold intensity also restricts the maximum allowed intensity of the incident laser beam. It is important to realize that the intensity strongly depends on the beam spot. Therefore, the positioning of the nonlinear crystals in relation to the focusing optics must take in to account the maximal intensity to prevent the destruction of the optical elements, the BBO crystal for example, and hence avoid the occurrence of additional nonlinear effects.

For the estimation of the placement of the optical elements, first the critical intensities have to be estimated. Using typical literature values that are summarized in Table 3.1, the value of critical intensity for white light generation $\frac{P_{cr}}{S}$ for sapphire crystal is the smallest, which makes it a good crystal for supercontinuum generation. At the same time it is possible to estimate that for our laser with the pulse energy $E = 200\ \mu$J and pulse duration $\tau = 600$ fs [15] the maximum intensity for a circular 1 mm diameter is:

$$\frac{P}{S} = \frac{E}{\tau\ S} \approx 0.33 \cdot 10^{11}\ \frac{W}{cm^2}\ , \tag{3.1}$$

which is below the threshold for the WLG in BBO but sufficient for the WLG in sapphire.

Medium	λ, nm	Pulse duration, fs	n_o	n_2, $\frac{cm^2}{W}$	I_{th}, $\frac{W}{cm^2}$	P_{cr}/S, $\frac{W}{cm^2}$
Sapphire [11, 26, 27]	1028	600	1.76	$3.2 \cdot 10^{-16}$	$3.8 \cdot 10^{12}$	$1.7 \cdot 10^{8}$
BBO [1, 2]	1028	600	1.66	$4.5 \cdot 10^{-20}$	$\sim 1 \cdot 10^{12}$	$\sim 17.7 \cdot 10^{11}$
Air [26, 27]	1028	600	~ 1	$4.7 \cdot 10^{-19}$	–	$3.37 \cdot 10^{11}$

Table 3.1: The optical properties of the used light propagation media. Here n_o is the ordinary refractive index, n_2 is the intensity-dependent refractive index, I_{th} the damage threshold and P_{cr} is white light generation critical power after Equation (2.41).

The Figure 3.3 shows the intensity profiles of a laser beam before and after a focusing lens with $f = 30$ cm. It is possible to see, that the damage threshold is not exceeded neither for the sapphire nor for the BBO before the lens. After the focussing the maximal intensity in the waist does not exceed the damage threshold of sapphire but is higher than the damage threshold of BBO. We used MATLAB (Chapter 5) to find the distances from the calculated beam waist where the damage threshold is still not exceeded. Assuming that the focal point coincides with the beam waist, the BBO crystals should be mounted not closer than 65 mm to the beam waist position.

3.1.3 Optimizing the phase matching angles

In Chapter 2 the condition of phase matching is mentioned as one of the main requirements of highly efficient nonlinear processes. It is important to note that for the collinear processes (SHG

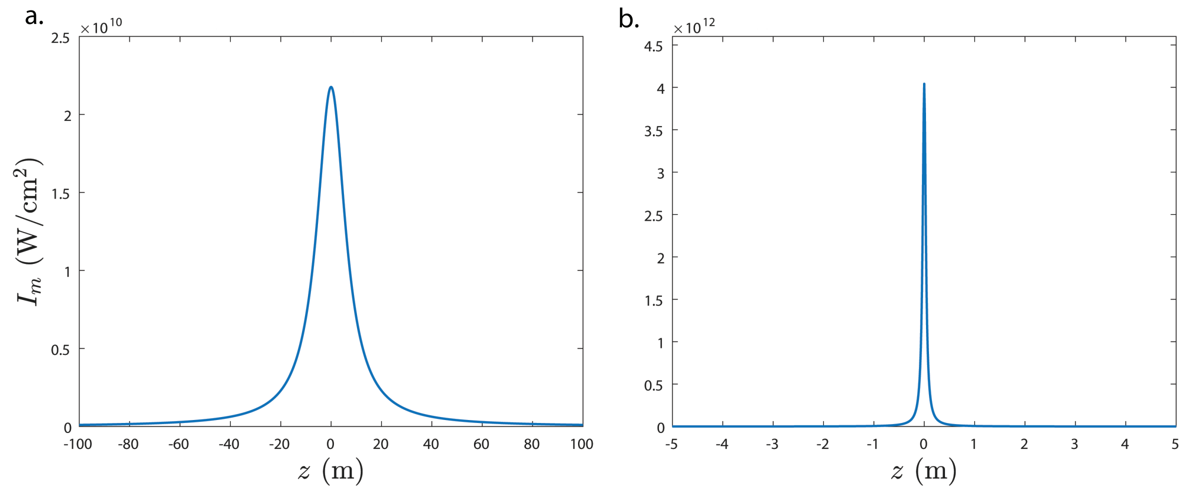

Figure 3.3: The intensity profiles of Gaussian beams before a focusing lens with $f = 30\,\mathrm{mm}$ (a.) and after it (b.) as function of the distances to the beam waists.

and THG) the BBO crystals are cut in such a way that the surface forms the angle $\beta = 90^o - \theta$ with the optical axis, where θ is the phase matching angle. The reason for this is to avoid the additional calculations for refraction effects because in this case the pump beams incident normally to the surface and take the angle θ with the optical axis. Table 3.2 shows the different mixing processes and the required polarization states of the beams as well as the phase matching conditions, for them and the matching angles calculated by our MATLAB script Chapter 5. The result of this calculation is shown in Figure 3.4 and Figure 3.6.

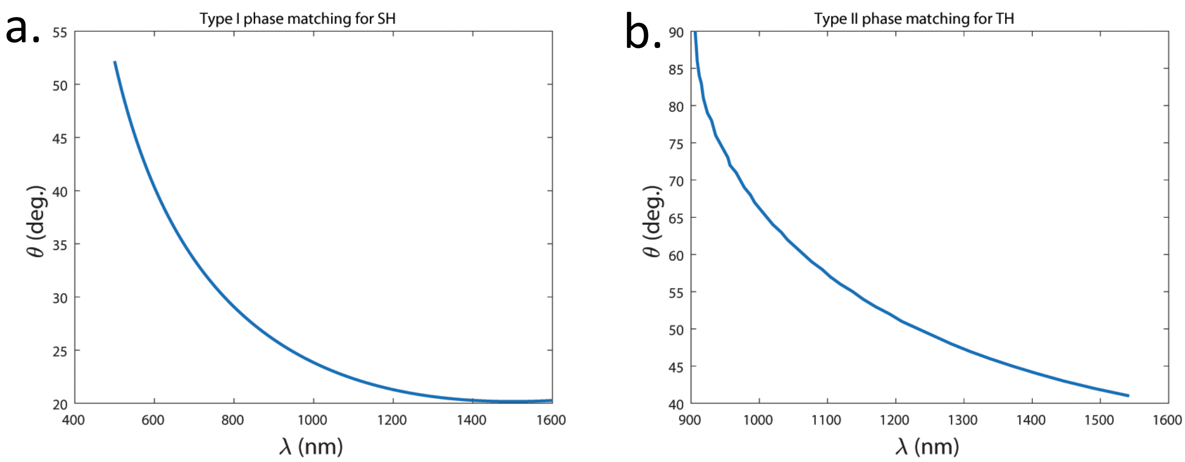

Figure 3.4: The dependences of the phase matching angle θ of the BBO crystal on incident light wavelength for second harmonic generation (a.) and third harmonic generation (b.).

The phase matching angle θ depends both on the signal wavelength and on the angle ϕ between the pump beams and the WL. But it is possible to find an angle ϕ such that the phase matching angle θ will be almost constant over the broad spectral range. The curves in the Figure 3.6(a. and b.) correspond to different angles ϕ from 0^o to 24^o for the 2ω-NOPA and 3ω-NOPA respectively. It is possible to see that the broadest spectrum can be obtained for $\phi = 5^o$ and $\phi = 7^o$ for 2ω-NOPA and 3ω-NOPA. It is important to note that this is the internal angle between the pump and signal laser beams inside the BBO. But of course if the beams incident to a BBO surface not at normal incidence, the angle between them will change due to Snell's law. For the NOPA branches we use two BBO crystals with the same cut ($\theta_o = 32.5^o$). According to the theoretical diagrams in Figure 3.6 we can assume that the internal angles between the optical axis and WL beam are equal to $\sim 32.5^o$ and $\sim 48^o$ for 2ω NOPA and 3ω NOPA, respectively. This values are different in comparison to, for example, Riedle and al works [13, 22] which is explained by the direction of the pump beam. The more common case is when the pump beam incidents from above into the BBO crystal therefore it forms the angle $\alpha = \theta + \phi$ with the optical axis of the crystal. In our case in both 2ω-NOPA and 3ω-NOPA the pump laser beams incident to a crystal from below and take an angle $\alpha = \theta - \phi$ with the optical axis of the BBO. We estimated the values of the external angles between pump and WL beams which are equal 8^o and 13^o respectively (Figure 3.5).

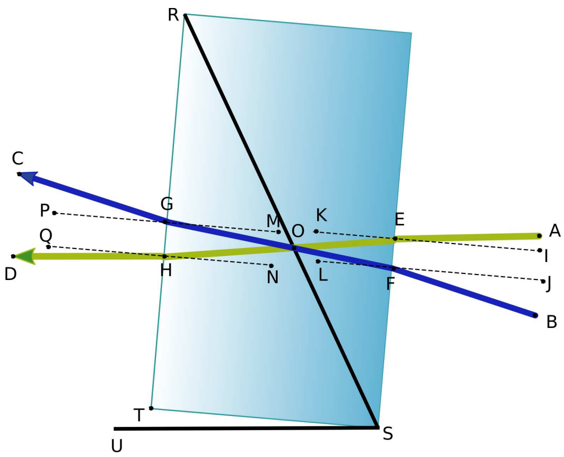

Figure 3.5: The detailed scheme of the incidence and propagation of the white light (greenish arrows) and the pump (blue arrows) laser beams in a tilted BBO crystal. The line RS represents the optical axis of the BBO crystal, dached lines: PM,QN,KI,LJ are perpendiculars to interfaces in the points of beam incidences: G,H,E,F. The angle RST is the BBO cut angle θ_o and the angle RSU is the phase matching angle θ. The internal noncollinear angle ϕ_{int} is the angle GOH or EOF, when the external noncollinear angle ϕ_{ext} is the angle between lines EA and FB.

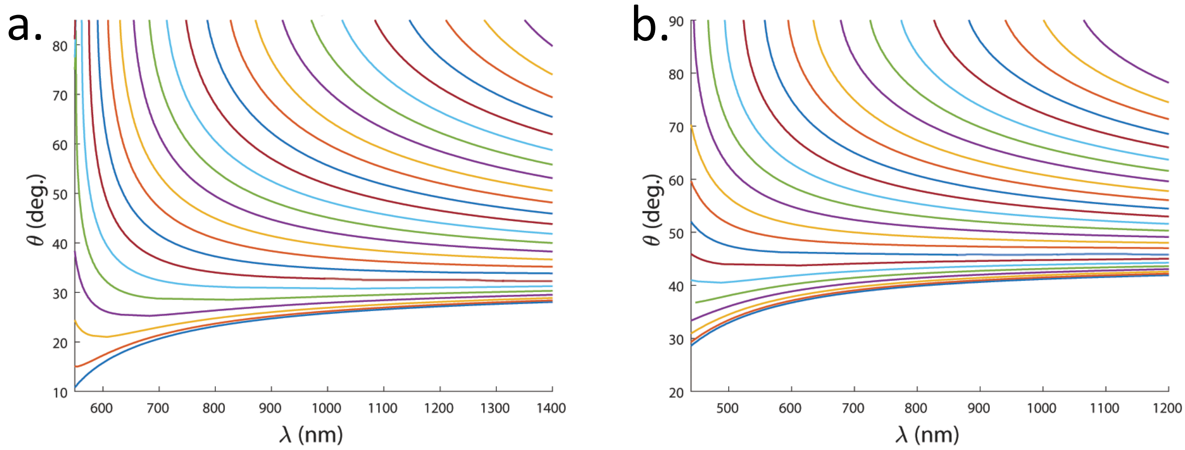

Figure 3.6: The dependences of the phase matching angle θ of the BBO crystal on incident light wavelength for different angles ϕ between the signal laser beam and pump laser beam for 2ω NOPA (a.) and 2ω NOPA (b.). Each curve corresponds to each value of ϕ where the lowest one corresponds to $\phi = 0^o$ and the highest to $\phi = 24^o$ with the step of 1^o.

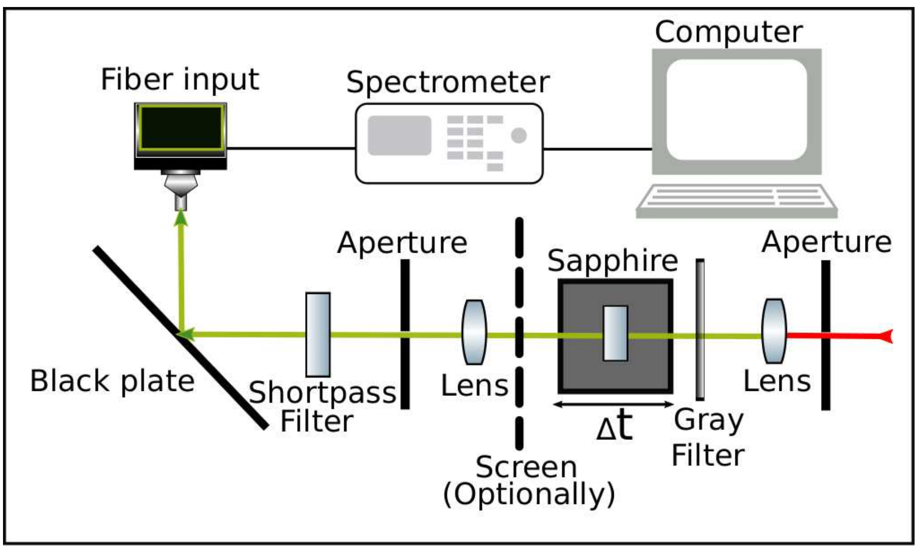

Figure 3.7: The principal scheme of the WLG, where the red beam is on the input.

Process	Configuration	Type	Phase matching condition	Phase matching angle θ
SHG	$o+o \rightarrow e$	Type I	$2 \cdot n_o(\omega) = n_e(2\omega, \theta)$	24^o
THG	$o+e \rightarrow e$	Type II	$n_o(\omega) + 2n_e(2\omega, \theta) = 3n_e(3\omega, \theta)$	66^o
NOPA	$e \rightarrow o+o$	Type I	$k_p = k_s \cos(\phi) + \sqrt{k_i^2 - k_s^2 \sin^2(\phi)}$	32.5^o (2ω), 48^o (3ω)

Table 3.2: The used configurations of polarisations, the phase matching conditions for them and the matching angles calculated by MATLAB script for each nonlinear process.

3.2 Adjustment and characterisation of the NOPA

3.2.1 Adjustment and characterisation of the white light generation

The WLG part of the scheme is presented in Figure 3.7. First we put a white screen after the sapphire crystal and set the gray filter to medium attenuation. After shifting the sapphire crystal into the focus of the collimated beam we start to decrease the level of attenuation of the gray filter. At one point a coloured spot appears on the screen (Figure 3.8). Then we iteratively shift the sapphire plate in one direction until the spot disappears or the intensity increases. Then the input power is either increased or decreased. Finally we search for the position and filter setting when the WL is generated with the minimum input power. We aim at the generation of the WL close to the back surface of the sapphire crystal as seen along the propagation direction of the input laser beam in order to diminish the influence of dispersion effects of the WL pulse. Then the stability of the WL spectrum is checked. A first optimization is done using our eyes but a more quantitative analysis is done using an Avantes AvaSpec spectrometer. Therefore the WL is coupled into a multimode fiber and spectrum analyzed by the spectrometer and displayed. Small optimizations should result in a temporally stable WL spectrum that also covers the broad spectral range between 400 and 700 nm. Often a reddish ring appears around the white spot, which is believed to be a sign of stable spectra and homogeneity [28]. For our spectral range however it is not necessarily helpful as it also indicates additional spectral components in the NIR region so we usually do not use this part and even block it using aperture A4. After putting the 300 nm - 700 nm short pass filter before the spectrometer we measure WL spectra similar to the one presented in Figure 3.9

3.2.2 Adjustment and characterization of the second and third harmonic generation

The principal scheme of the second and the third harmonic generation is shown in Figure 3.1. It consists of the two lenses L1 ($f = 300$ mm) and L2 (f=150 mm), that focus the fundamental laser beam between the BBOs and collimate the generated 2ω and 3ω beams respectively. Two BBO with special cuts (see Section 3.2.3) are used for the SH and TH generation and two dichroic mirrors separate the SH and TH fromthe non-converted fundamental laser wavelength. For the

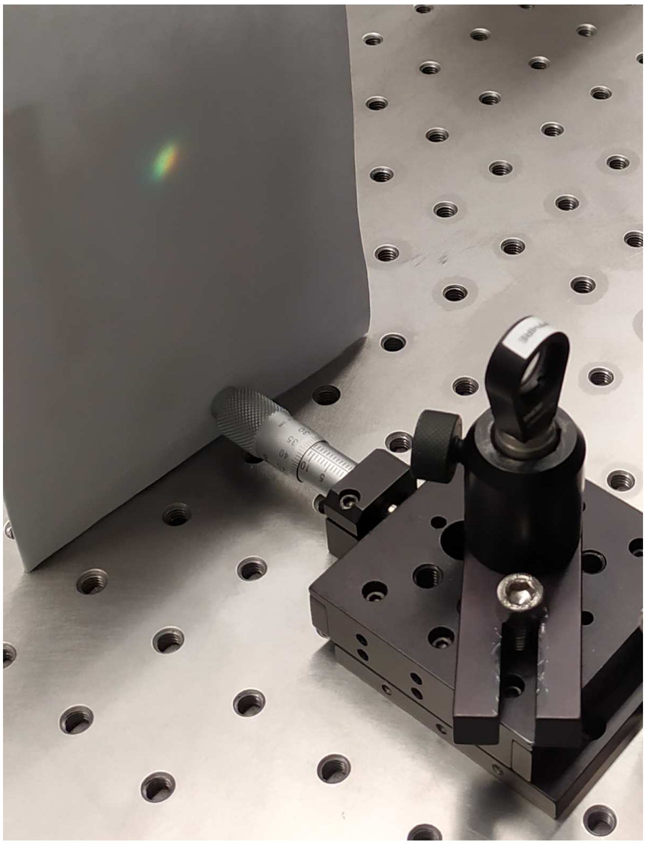

Figure 3.8: The photo of the white light spot projected on the sheet of paper placed after the sapphire crystal.

basic alignment in the beginning we put the BBO I 9 cmbefore the focus of L1. After that we but a black screen after the second lens. If the BBO crystal is put in the right orientation, it almost immediately generates the green SH light even with reduced average laser power; for the alignment we use the pulse picker of the Pharos laser that allows us to reduce the average laser power but maintains the pulse energy. After this we put in the dichroic mirror DM1 in order to measure the power of the generated SH light with the power meter. We are aiming at the maximum efficiency of the generation for this position of the BBO crystal so we tweak the tilt angle and slightly rotate the BBO in its mount until we obtain the maximum power of the converted light. When this is done, we put in the second BBO II in the distance of 9 cm after the focus of L1. As in the previous case, if the BBO II is put in the right orientation, the TH light can be observed on a white paper due to the induced fluorescence. We usee DM2 to reflect only the TH light to the powermeter head and optimize the orientation of BBO II until we obtain the maximum conversion efficiency.

In Figure 3.10 we show the spectra of the SH and TH light after the reflection of the respective dichroic mirrors. The observed power of the beams is 2.7 W and 1.6 W respectively. Taking into account that the incident power before the first BBO is 12.4 W, the efficiency of SHG and THG

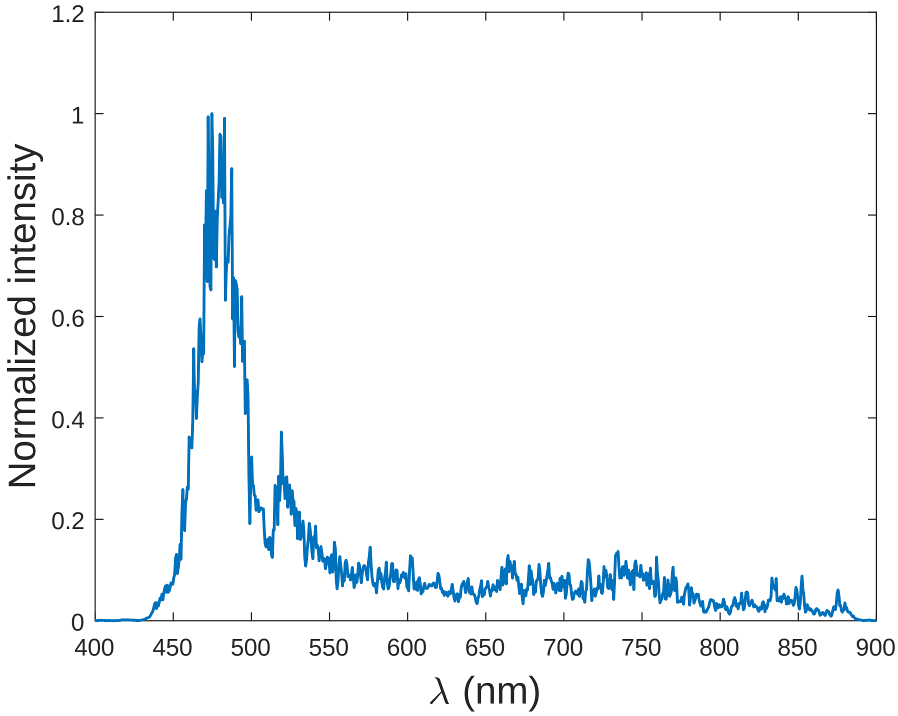

Figure 3.9: Typical white light spectrum as generated in a sapphire crystal and filtered by a 300 nm - 700 nm short-pass filter.

amounts to $\eta_{SHG} = 22\%$ and $\eta_{THG} = 13\%$, consistent with our previous experiences and the data reported in [13, 22]. For the use as the NOPA pump beams, the SH and TH light is redirected to the NOPA branches by the flat mirrors (M12, M13) and focussed into BBO III and BBO IV with the spherical mirrors FS1 and FS2. Finally, the power that is available for pumping the BBO crystals in the NOPA branches is slightly reduced to 2.15 W for 2ω-NOPA and 1.25 W for 3ω-NOPA.

3.2.3 Adjustment and characterisation of the 3ω NOPA branch

The noncolinear optical parametric amplification allows not only to amplify the weak signal (in our case given by the WL), but is also accompanied by the generation of the strong idler beam (see Section 2.1.5). For the proposed 3ω-NOPA the generated idler is in the visible spectral range (Figure 3.6), thus the begin of the amplification is rather easy to detect directly by eye.

The crucial requirement for obtaining the optical parametric amplification is the temporal overlap of pump and signal pulses. To satisfy the temporal overlap at first we try to make the optical paths of the WL and 3ω pump laser beams equal with a ruler. The translation (delay) stages are then put to in their arbitrary neutral positions to allow us being more flexible in further precise adjustments. After that we used an ultrafast photodiode (Thorlabs DET025A/M, response

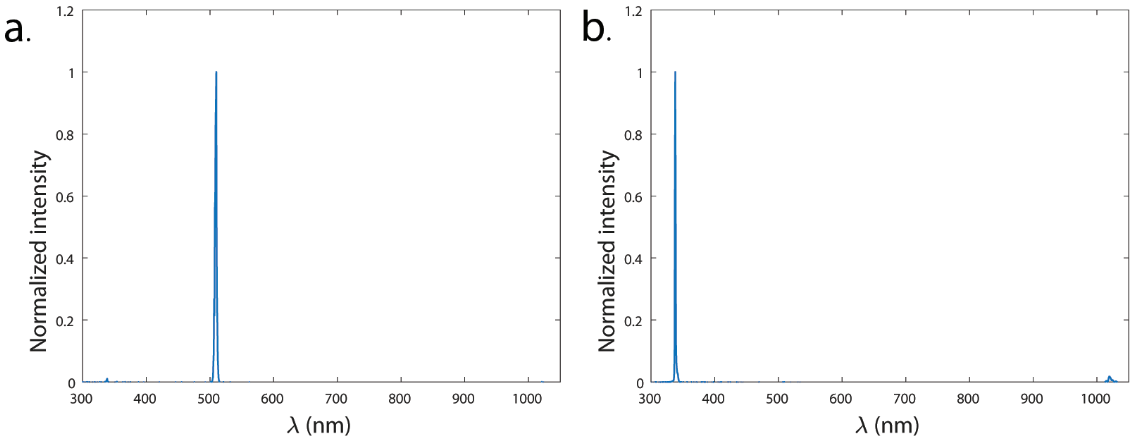

Figure 3.10: The spectra of the SH beam reflected from the dichroic mirror DM1 (a.) and the TH beam reflected from DM2 (b.)

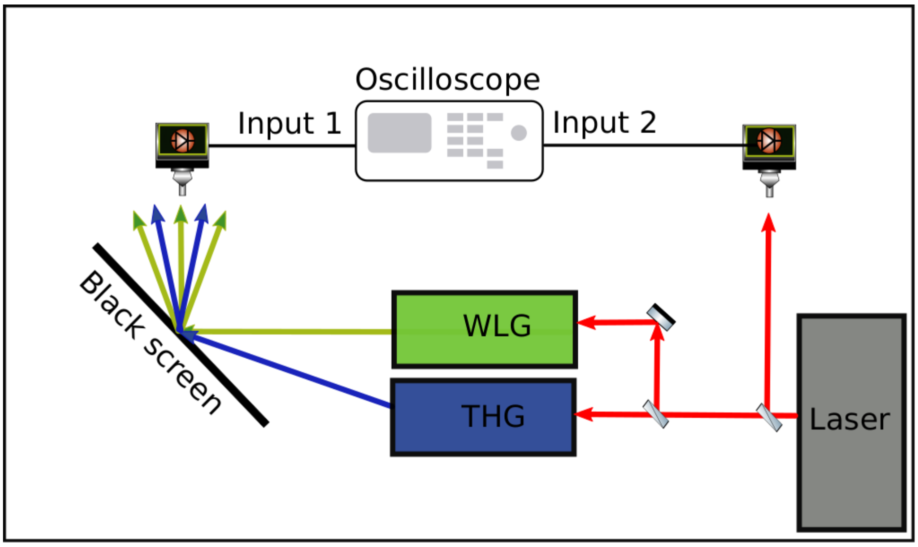

Figure 3.11: The optical scheme for the defining of temporal delay between 3ω pump laser pulse and white light laser pulse.

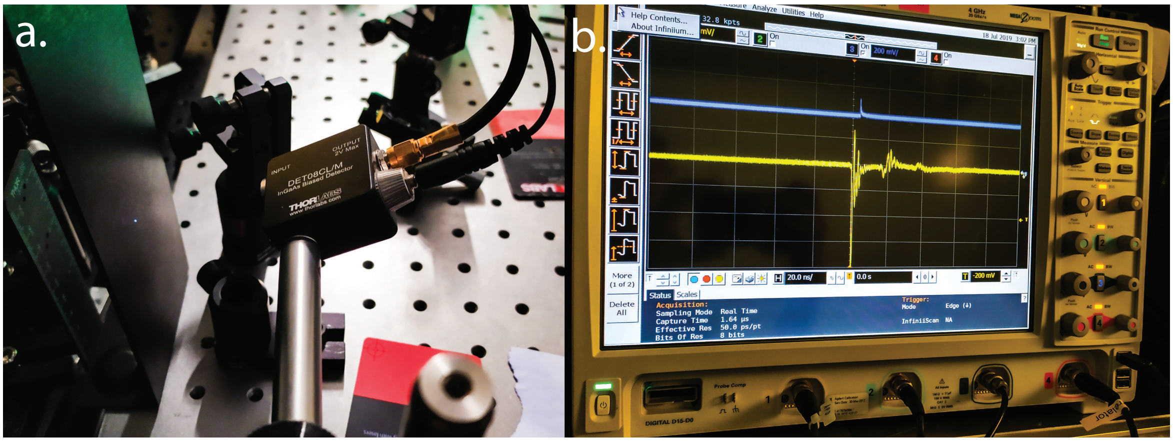

Figure 3.12: The photo of time overlap measurement scheme (a.) and correspondent oscilloscope signal (b.) .

time approximately 150, ps), which was connected to an Agilent DSO9404A oscilloscope. The light is reflected from a black screen placed at the position of BBO IV. This scheme is shown in Figure 3.11 and Figure 3.12. As reference trigger we use the light reflected from a beamsampler right after the laser output using a biased avalanche laser diode (Hamamatsu) connected to the oscilloscope. This allows us to measure the time delay between the arrival of the WL and the 3ω pump at the same position. Our task is now make the delay between both pulses 0 using the delay stages. This was done iteratively and required also the slight repositioning of optical elements.

Now we place BBO IV on a translation stage in a distance of 5 cm after the focus of the focusing mirror FM2. We direct the 3ω pump beam to the center of BBO IV tweaking the focusing mirror FM2 and the plane mirror M13. If the BBO crystal is properly oriented and the phase matching angle is correct for the pump wavelength, the pump photons decay randomly in different directions into pairs with different frequencies and therefore the so-called superfluorescence cone is generated. This appears as broad colored ring on the screen as shown in Figure 3.13 (a.) and (b.), where the colors are split like in a rainbow. Tilting the BBO along its horizontal axis allows to obtain a thin almost white ring consisting of all of colors, which means that now we fulfil the condition for the broad spectral range of the pump photon decay that is reflected in the desired curves shown in Figure 3.6. For our case of the 3ω NOPA we obtain the white ring with orange tint shown in Figure 3.13 (c.) and (d.).

Another crucial point for the operation of the NOPA is the spatial overlap between WL and pump pulses. After obtaining the narrow superfluorescence ring we open the WL beam and direct it to the center of the BBO and overlap it with the spot of the pump beam. This results in the projection of the superfluorescence cone and the WL spot on the screen. Since the WL is the seed for the pump photon split we need to overlap both of these projections without loosing the temporal or spatial overlap between the two beams in the BBO. In order to do this we iteratively tilt the flat mirror M13 along the horizontal axis and then tilt the focusing mirror FM2 to bring back the overlap in BBO IV. Finally we tilt the BBO crystal to maintain the narrow superfluorescence ring on the screen. If the direction of the tilting is chosen correctly, it is possible to see at one point the overlap of the projections on the screen. While trying to keep the temporal

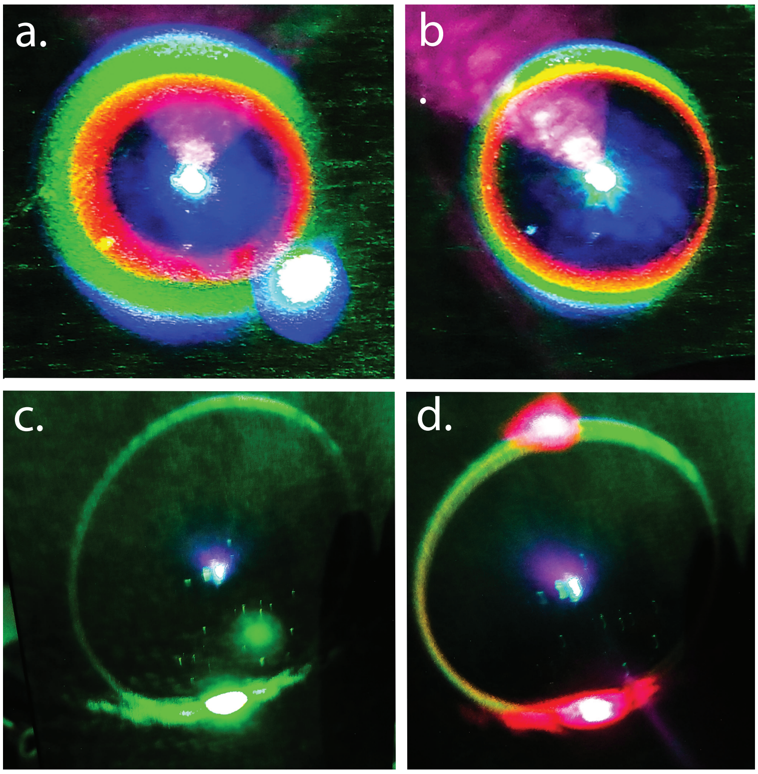

Figure 3.13: The projections of the broad super fluorescence ring and the white light beam (a.), medium thickness super fluorescence ring (b.), narrow super fluorescence ring with the amplified green light and invisible IR idler (c.), narrow super fluorescence ring with the amplified red light and red idler (d.) on the black screen.

overlap condition we have to slightly change the position of the delay stage and find that the intensity of the superfluorescence ring reduces while the WL spot becomes brighter and changes its color and another bright spot appears on the upper side of the superfluorescence ring, which is seen in Figure 3.13 (c.) and (d.). This is the clear signature of the parametric amplification.

3.2.3.1 Spectral characterization of the 3ω NOPA

After the first amplification was obtained as described in the section before, we included an aperture behind BBO IV that blocks all unwanted beams except of the amplified signal and place the head of the powermeter behind the aperture. Then it is possible to optimize the BBO tilt, the spatial overlap in it, and its optimum position in relation to the focus of FM2. When we reach an amplification of different wavelengths, we remove the powermeter and put the black screen back

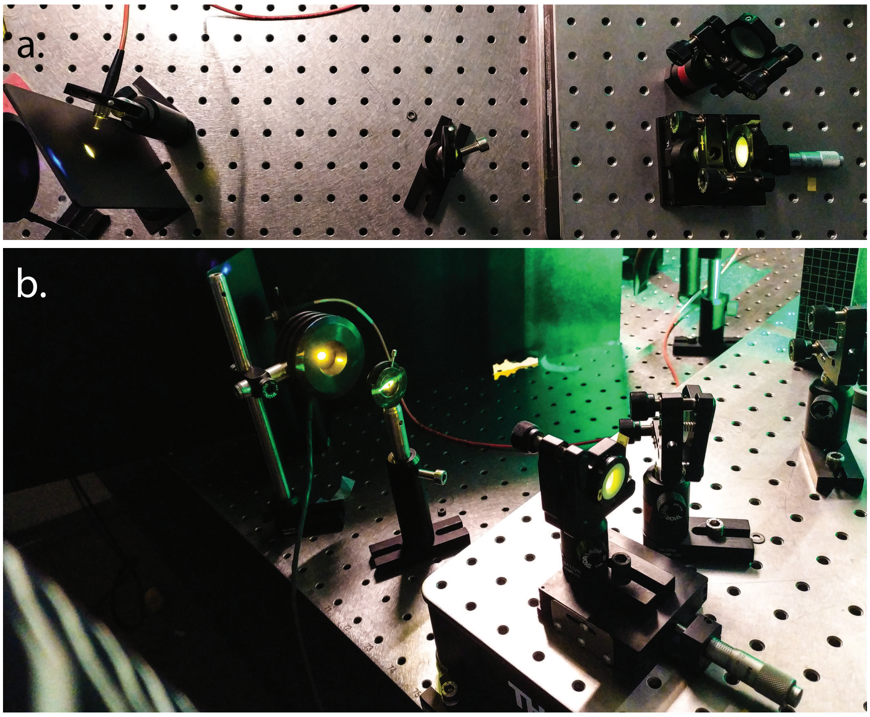

Figure 3.14: The photos of the 3ω-NOPA pulse specta (a.) and power (b.) measurement processes.

and measure the spectra of the 3ω-NOPA pulses scattered from the screen using the spectrometer (Figure 3.14 (a.)), similarly as we do it for the WL spectrum displayed in Section 3.2.3. The spectra are measured for different positions of the FM2 translation stage between 0 to 25 μm with the step width of 2.5 μm, which then converted to the temporal scale from 0 fs to 1650 fs. The spectra are shown in Figure 3.15.

One immediately sees that the FWHM of the 3ω-NOPA pulses are different in relation to the central wavelength. Assuming that all of these spectra exhibit a Gaussian profile it is possible to estimate the Fourier limit of the pulses and obtain their duration $\Delta\tau$:

$$\Delta\tau = \frac{K}{c\Delta\lambda}\lambda^2 \ . \tag{3.2}$$

Here $K = 0.44$ is the parameter for a Gaussian line shape, λ is central wavelength of the pulse, $\Delta\lambda$ is the FWHM of the pulse, and c is the speed of light in vacuum. As one might expect, spectrally broader pulses correspond to temporally shorter pulses. The calculated values of of $\Delta\tau$ as function of the central wavelength is presented in Figure 3.16. One immediately notices that the 3ω-NOPA pulses are significantly shorter than the laser output pulse duration is 600 fs. The minimum number of 10 fs is likely an artefact because of the assumption that theses pulses have a Gaussian line shape. Already the raw spectra shown in Figure 3.15 show that in broadest pulses are not Gaussian anymore.

Another important parameter of the NOPA pulses is their power. To characterise the 3ω-NOPA output we again put the head of the powermeter after the aperture and measure the

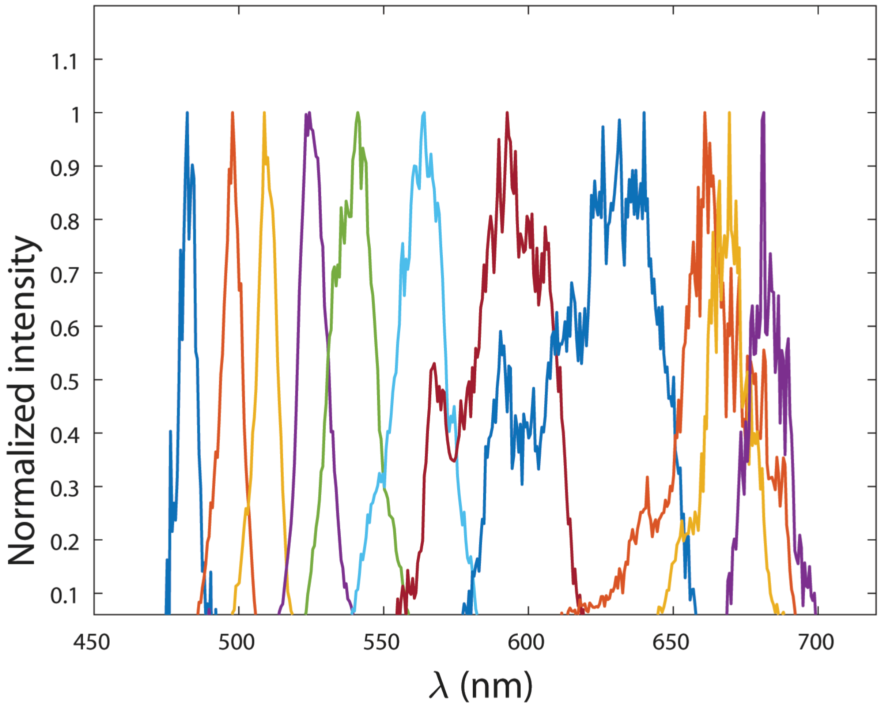

Figure 3.15: The normalized spectra of the 3-ωNOPA output for different positions of the focusing mirror FM6 on the translation stage. The spectra correspond to time-delays of 0; 165 fs; 330 fs; 495 fs; 660 fs; 825 fs; 990 fs; 1155 fs; 1320 fs; 1485 fs; 1650 fs between the white light and the 3ω pump laser beams.

power of the amplified pulses shown before (Figure 3.14 (b.)). The absolute power of the pulses strongly depends on the diameter of the aperture and its position, so we make a series of the measurements where the parameters of the aperture and the position of the powermeter are kept constant. The dependence of the pulse power on the central wavelength of the pulse is shown in Figure 3.17. As one can see the power reaches the maximum constant values around 16 mW for the range between 540 nm and 640 nm. It is possible to change the profile of this dependence due to the BBO tilt, which allows to enhance amplification for different wavelengths, if desired. Our aim is to amplify a broad spectral range, thus the amplification efficiency is not maximum.

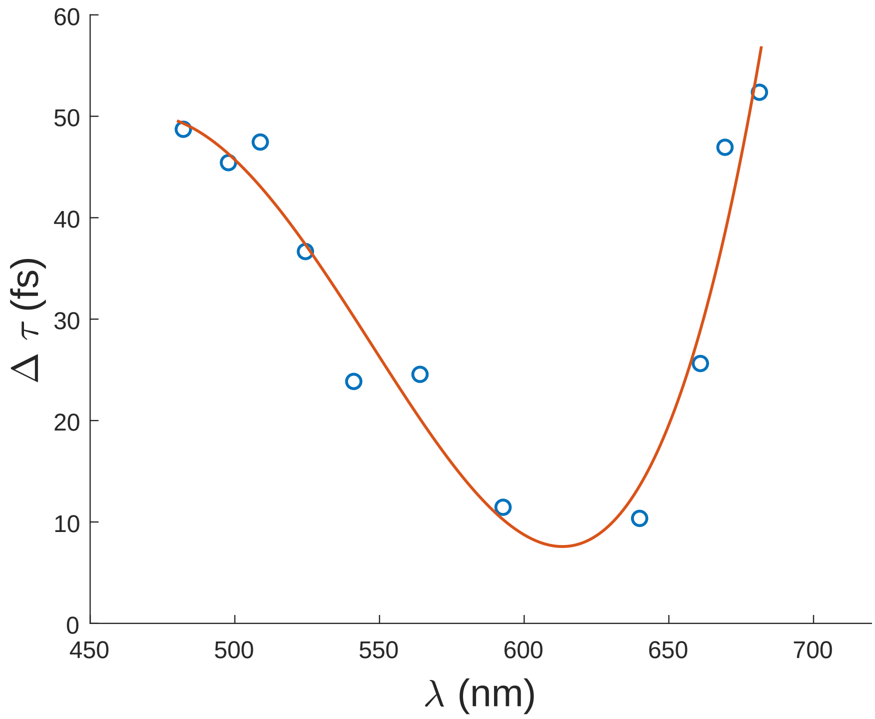

Figure 3.16: The dependence of the 3ω-NOPA pulse durations on central pump wavelength. Circles correspond to the Fourier limit data calculated from the experimentally measured 3-ωNOPA pulse spectra. The red solid line serves as guide to the eye.

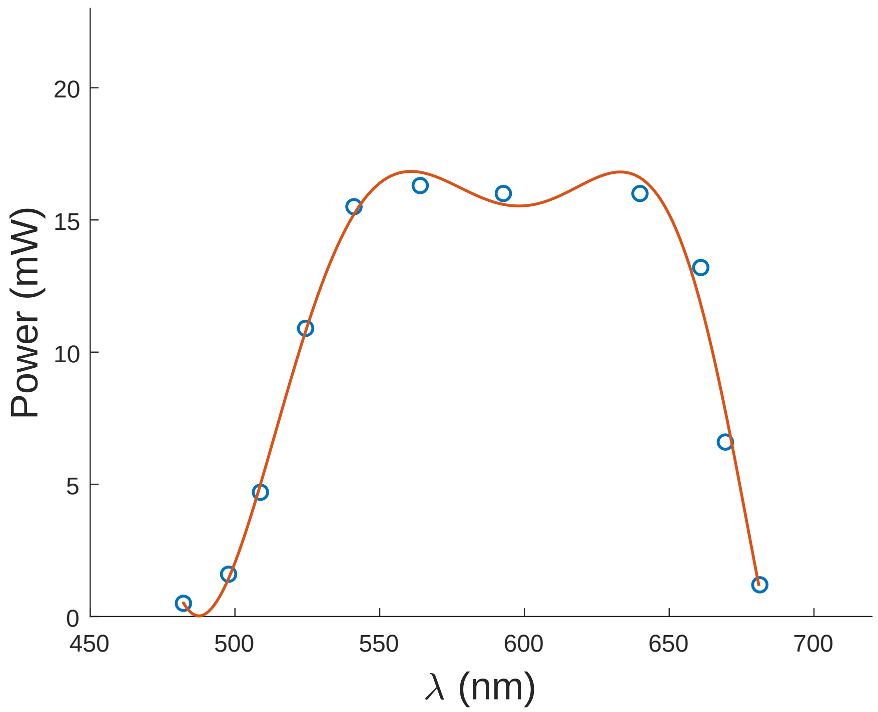

Figure 3.17: The dependence of the 3ω-NOPA pulse power on the central pump wavelength. Circles correspond to the experimental data and the red line is a guide to the eye.

Chapter 4

Conclusions

There are several of nonlinear processes which take place in our NOPA: second harmonic generation due to frequency doubling, third harmonic generation due to sum frequency generation, white light supercontinuum generation, and noncolinear optical parametric amplification. The efficiency of generation and amplification depends on meeting the conditions of phase matching, spatial and temporal overlap of the interacting laser pulses. The phase matching condition can be also either fulfilled in a collinear or noncollinear arrangement. In this work we briefly described the main theoretical principles of nonlinear processes that are important for our NOPA. The two stage NOPA was designed in accordance with the conditions of restricted place, transportability, and a broad spectral range of output wavelengths. The calculations for the optimal phase matching angles, noncollinearity angles, and the distances at which the optical elements should be placed for optimum efficiency but without their destruction, were calculated and the consequences explained. During the setup of the NOPA the second harmonic and third harmonic of the pump beams for the NOPA were built and optimized. The spectra efficiency of the pump beams were measured. A stable white supercontinuum light was generated in a sapphire crystal that serves as seed for the NOPA branches. The spatial and temporal overlap between white light and third harmonic were found and the 3ω-noncollinear optical parametric amplification process was optimized. Finally, the output of the 3ω-NOPA was characterized and pulses with the power up to 17mW in a 475 nm – 700 nm spectral range were measured. The Fourier limit of 3ω-NOPA pulses was also found, therefore their calculated durations are much shorter than 600 fs input beam and vary between 50 fs and 10 fs.

In addition, all of the adjustment processes were explained in detail, so it will be possible to use this internship report as a guide for the building and adjustment of new NOPAs, for example for the realization of the 2ω NOPA branch.

BIBLIOGRAPHY

[1] M. BACHE, H. GUO, B. ZHOU, AND X. ZENG, *The anisotropic Kerr nonlinear refractive index of the beta-barium borate (\beta-BaB2O4) nonlinear crystal*, (2012).

[2] G. C. BHAR, A. K. CHAUDHARY, P. KUMBHAKAR, A. M. RUDRA, AND S. C. SABARWAL, *A comparative study of laser-induced surface damage thresholds in BBO crystals and effect of impurities*, Optical Materials, 27 (2004), pp. 119–123.

[3] M. U. BILYY, *Fundamentals of nonlinear optics and its applications*, VPC "Kyiv University", 1999.

[4] N. BLOEMBERGEN, *Nonlinear optics 21.1 21.2*, Media, (1981), pp. 873–917.

[5] R. W. BOYD, *Nonlinear optics*, Academic Press, 3rd. ed., 2008.

[6] A. BRODEUR AND S. L. CHIN, *Ultrafast white-light continuum generation*, 16 (1999).

[7] B. CHANCE, *The accelerated flow method for rapid reactions*, Journal of the Franklin Institute, 229.6 (1940).

[8] CHELSEY DOROW, *An Introduction to the Technique and Applications of Pump-Probe Spectroscopy*, Special Topic Paper, Physics 211A.

[9] A. DUBIETIS, G. TAMOŠAUSKAS, R. ŠUMINAS, V. JUKNA, AND A. COUAIRON, *Ultrafast supercontinuum generation in bulk condensed media (Invited Review)*, (2017).

[10] G. M. GALE, M. CAVALLARI, T. J. DRISCOLL, AND F. HACHE, *Sub-20-fs tunable pulses in the visible from an 82-MHz optical parametric oscillator*, Optics Letters, 20 (2008), p. 1562.

[11] I. GRAŽULEVIČIŪTĖ, M. SKEIVYTĖ, E. KEBLYTĖ, J. GALINIS, G. TAMOŠAUSKAS, AND A. DUBIETIS, *Supercontinuum generation in YAG and sapphire with picosecond laser pulses*, Lithuanian Journal of Physics, 55 (2015), pp. 110–116.

[12] "HELMHOLTZ ZENTRUM BERLIN OFFICIAL SITE", *Synchrotron Radiation at BESSY II*.

[13] C. HOMANN, C. SCHRIEVER, P. BAUM, AND E. RIEDLE, *Octave wide tunable UV-pumped NOPA: pulses down to 20 fs at 0.5 MHz repetition rate*, Optics Express, 16 (2008), p. 5746.

[14] Y. N. KULCHIN AND Y. N. KULCHIN, *Fundamentals of Nonlinear Optics*, Modern Optics and Photonics of Nano and Microsystems, (2018), pp. 1–40.

[15] LIGHT CONVERSION, *Pharos Laser datasheet*, 2018.

[16] MAX BORN AND EMIL WOLF, *Principles of optics Electromagnetic theory of propagation, interference and diffraction of light with contributions*, (2003), p. 936.

[17] R. MENZEL, *Photonics. Linear and Nonlinear Interactions of Laser Light and Matter*, Springer Berlin Heidelberg, Berlin, 2nd ed., 2001.

[18] D. MESCHEDE, *Optics, Light and Lasers: The Practical Approach to Modern Aspects of Photonics and Laser Physics. By Dieter Meschede.*, vol. 6, 2004.

[19] E. R. PETER BAUM, STEFAN LOCHBRUNNER, PATRIZIA KROK, MARKUS BREUER, *NOPA - overview and principles*.

[20] G. PORTER, *Flash photolysis and spectroscopy. A new method for the study of free radical reactions.*, Proceedings of the Royal Society of London, Series A. (1950).

[21] P. RUELLO AND GUSEV V. E., *Physical mechanisms of coherent acoustic phonons generation by ultrafast laser action*, Ultrasonics, 2015 Feb;5.

[22] C. SCHRIEVER, S. LOCHBRUNNER, P. KROK, AND E. RIEDLE, *Tunable pulses from below 300 to 970 nm with durations down to 14 fs based on a 2 MHz ytterbium-doped fiber system*, Optics Letters, 33 (2008), p. 192.

[23] S. A. SELF, *Focusing of spherical Gaussian beams*, Applied Optics, 22 (2009), p. 658.

[24] Y. R. SHEN, *The principles of Nonlinear Optics*, A Wiley-Interscience Publication, Berkeley, 1984.

[25] R. L. SUTHERLAND, D. G. MCLEAN, AND S. KIRKPATRICK, *Handbook of Nonlinear Optics with contributions by*, 2003.

[26] O. UTEZA, B. BUSSIÈRE, F. CANOVA, J.-P. CHAMBARET, P. DELAPORTE, T. ITINA, AND M. SENTIS, *Damage threshold of sapphire in short and long pulse regime*, International Conference on Lasers, Applications, and Technologies 2007: Laser-assisted Micro- and Nanotechnologies, 6732 (2007), p. 67321P.

[27] O. UTEZA, B. BUSSIÈRE, F. CANOVA, J. P. CHAMBARET, P. DELAPORTE, T. ITINA, AND M. SENTIS, *Laser-induced damage threshold of sapphire in nanosecond, picosecond and femtosecond regimes*, Applied Surface Science, 254 (2007), pp. 799–803.

[28] K. WILSON, *Guide to Nopas From the Mccamant Group at the University of Rochester*, (2000), pp. 1–17.

Matlab Code for the defining of the positions of BBO crystals

```
%input parameters
f=300*10^(-3);              %focal length m
lambda=1028*10^(-9);        %wavelength m
w_o=1.5*10^(-3);            %input waist m
z_o=650*10^(-3);            %position of the input waist m (from laser to
    the waist)
L=1700*10^(-3);             %total length between laser and first length
s=L-z_o;                    %waist to len s distance
E=200*10^(-6);              %pulse energy (joules)
tau=600*10^(-15);           %pulse duration (seconds)
P=E/tau;                    %pulse power (joules per sec)
I_cr=10^12;                 % W/cm^2 %critical value of intensity for BBO
P_cr=17.7 * 10^(9)          %white light cr. power

%programing
z=-100000:0.5:100000; z=z/1000;                  %scale from the both
    sides of the waist +-100m

z_r=pi*(w_o)^2/lambda;                           %Raleigh dist
w=w_o*sqrt(1+(z/z_r).^2);                        %Beam radius on z

%%
figure(1);
plot(z,w*1000);
title('Values of the beam radius before focusing');
xlabel('distance,meter');
ylabel('beam radius,mm');

```

```

I_zenter=(2*P/pi)./(w.*w);                          %intensity in the center of gaussian
figure(2);
plot(z,I_zenter/10000);
axis auto
%axis([-0.15 0.15 0 4.6*10^4 ]);
title('Values of max gaussian intensity before focusing');
xlabel('distance,meter');
ylabel('center intensity, W/(cm^2)');



%finding the position where the max Intesity of Gaussian will be the most
%close to the BBO damage intensity

j=0;                                                %index of searched value in array
k=10^20;                                            %starting difference which is infinity
for i=200001:400001                                 %use only one side from the focus (o to 100m)
    if abs(I_zenter(i)-I_cr)<=k                     %if the value is closer to critical then we need it
        k=abs(I_zenter(i)-I_cr);
        j=i;
    end
end
z_cr=z(j);                                          %the distande between waist and the critical value of intensity


j=0;                                                %index of searched value in array
k=10^20;                                            %starting difference which is infinity
for i=200001:400001                                 %use only one side from the focus (o to 100m)
```

```
    if abs(pi*w(i)*w(i)*I_zenter(i)/2-P_cr)<=k                    %if the value is closer to critical then we need it
        k=abs(pi*w(i)*w(i)*I_zenter(i)/2-P_cr);
        j=i;
    end
end
zp_cr=z(j);                                   %the distande between waist and the critical value of intensity




%after focusing


s1=f*(1+(s/f - 1)/((s/f - 1)^2+(z_r/f)^2));     %position of focused waist
w_o=w_o/sqrt(1-(s/f)^2+(z_r/f)^2);             %new size of focused waist
z_r=pi*(w_o)^2/lambda;                         %new Raleigh dist
w=w_o*sqrt(1+(z.^2/z_r/z_r));                  %new Beam radius on new z





figure(3);
plot(z,w*1000);
axis auto
%axis([-0.01 0.01 0.04 0.1]);
title('Values of the beam radius after focusing');
xlabel('distance,meter'); ylabel('beam radius,mm');


I_zenter=(2*P/pi)./(w.*w);                     %intensity in the center of new gaussian
figure(4);
plot(z,I_zenter/10000);
```

```
%axis auto
axis([-5.0 5.0 0 4.6*10^12 ]);
title('Values of max gaussian intensity after focusing');
xlabel('distance,meter');
ylabel('center intensity, W/(cm^2)');


I_ooo= 10^(12)/w_o/w_o*w(200301)*w(200301);
E_ooo=I_ooo*260*10^(-15)*w(200301)*w(200301);
%finding the new position where the max Intesity of Gaussian will be the most
%close to the BBO damage intensity

j=0;                                         %index of searched value in array
k=10^20;                                     %starting difference which is infinity
for i=200001:400001                          %use only one side from the focus (o to 100m)
    if abs(I_zenter(i)/10000-I_cr)<=k             %if the value is closer to critical then we need it
        k=abs(I_zenter(i)/10000-I_cr);
        j=i;
    end
end
z_cr1=z(j);                                  %the new distande between waist and the critical value of intensity
```

Matlab Code for the defining the phase matching and noncollinearity angles

```
%% n_o and n_e as a function of wavelength
lambda=(250.0000:0.5000:1600.0000); %wavelength nanometers  VVVVVERIFIED
no=sqrt(2.7366122+0.0185720./((lambda/1000).^2-0.0178746)-0.0143756*(
    lambda/1000).^2);
ne=sqrt(2.3698703+0.0128445./((lambda/1000).^2-0.0153064)-0.0029129*(
    lambda/1000).^2);
figure(1);
plot(lambda,no,'LineWidth',2);
axis auto
hold on
plot(lambda, ne,'LineWidth',2);
%title('upper no and lower ne');
axis auto
hold off
xlabel('\lambda (nm)',  'FontSize', 16);
ylabel('n',  'FontSize', 16);

%%  n_e as a function of angle
T=(0:90);
T=T/360*2*pi;
ne_t=zeros(2701,91);
 for i=1:2701
     for j=1:91
         ne_t(i,j)=no(i)*ne(i)/sqrt(no(i)^2*(sin(T(j)))^2+ne(i)^2*(cos(T(j
             )))^2);
     end
 end
T=T*360/2/pi;
figure(2);
plot(T,ne_t(1,:));
title('ne for different angles (wavelength 250 nm)')
axis auto
```

```
%% elipsoid for indexes of refr.
figure(3)
[x, y, z] = ellipsoid(0,0,0,no(1557),no(1557),no(1557));
surf(x, y, z)
axis equal
hold on

[x, y, z] = ellipsoid(0,0,0,ne(1557),ne(1557),no(1557));
surf(x, y, z)
title('inner ellips. for ne, outer for ne for 1028 nm')
xlabel('n_x');
ylabel('n_y');
zlabel('n_z');



%% SHG Type 1 (ooe) in BBO
Teta=zeros(1001,1); Teta=Teta';
lambda_cut=(250:0.5:800);
for i=501:2:2701
    ii=0.5*(i+1)-250;
    Teta(ii)=asin(ne(ii)/no(i)*sqrt((no(ii)^2-no(i)^2)/(no(ii)^2-ne(ii)^2)));
end
lambda_cut=lambda_cut*2;
Teta=Teta*360/2/pi;
figure(4);
plot(lambda_cut, Teta,'LineWidth',2);
title('Type I phase matching for SH')
xlabel('\lambda (nm)',  'FontSize', 16);
ylabel('\theta (deg.)', 'FontSize', 16);
axis auto



%% SFG Type 2 (eoe) in BBO
w3_massive=zeros(284,2);
%T=T/360*2*pi;
```

```
delt=100000;
for i=1002:6:2700

    for k=1:91

 a=abs(no(i-1)+2*ne_t(i/2-250,k)-3*ne_t((i+501)/3-501+1,k));
        if a<delt
            delt=a;
            index=k;
        end
    end
    w3_massive((i-1002)/6+1,1)=lambda(i-1);
        w3_massive((i-1002)/6+1,2)=T(index);
    delt=100000;
    index=100000;
end
zzz= zeros(45,2);
m=1;
for i=1:283
    if (abs(w3_massive(i,2)-w3_massive(i+1,2))>=0.00001)
      zzz(m,1)=w3_massive(i,1);
      zzz(m,2)=w3_massive(i,2);
     m=m+1;
    end
end
figure(5);
plot(zzz(:,1), zzz(:,2),'LineWidth',2);
title('Type II phase matching for TH')
xlabel('\lambda (nm)',  'FontSize', 16);
ylabel('\theta (deg.)', 'FontSize', 16);
axis auto
 %% 3w NOPA phase matching Type 1 ooe in BBO
T=(0:0.25:90);
T=T/360*2*pi;
omega=zeros(2701,1);
omega=(1./lambda).*100000000;
ffi_theta_lambda_massive=zeros(2326,361);
Fi=(0:90); T=T/360*2*pi; Fi=Fi/360*2*pi;
```

```
wp=1/343*100000000;
d=100000;
for m=1:2701
    a=abs(omega(m)-wp);
    if a<d
        d=a;
        index_pump=m;
    end
end
for j=1:91
    for i=375:2701
        delta=10000000000000000;
        wi=wp-omega(i);
        d=1000000000000;
        index_k=1;
        index=1;
        for m=1:2701
            a=abs(omega(m)-wi);
            if a<d
                d=a;
                index=m;
            end
        end
        for k=j:361
            a=abs((wp*ne_t(index_pump,k-j+1))^2+(omega(i)*no(i)*cos(Fi(j)))^2-2*wp*omega(i)*cos(Fi(j))*ne_t(index_pump,k-j+1)*no(i)-(wi*no(m))^2+(omega(i)*no(i)*sin(Fi(j)))^2)
            if a<delta
                delta=a;
                index_k=k;
            end
        end
        ffi_theta_lambda_massive(i-374,j)=T(index_k)/2/pi*360; %%vylazit za predely
    end
end
figure(6);
plot(lambda(375:2701),ffi_theta_lambda_massive(:,1));
```

```
hold on
plot(lambda(375:2701),ffi_theta_lambda_massive(:,2),'LineWidth',2);
plot(lambda(375:2701),ffi_theta_lambda_massive(:,3),'LineWidth',2);
plot(lambda(375:2701),ffi_theta_lambda_massive(:,4),'LineWidth',2);
plot(lambda(375:2701),ffi_theta_lambda_massive(:,5),'LineWidth',2);
plot(lambda(375:2701),ffi_theta_lambda_massive(:,6),'LineWidth',2);
plot(lambda(375:2701),ffi_theta_lambda_massive(:,7),'LineWidth',2);
plot(lambda(375:2701),ffi_theta_lambda_massive(:,8),'LineWidth',2);
plot(lambda(375:2701),ffi_theta_lambda_massive(:,9),'LineWidth',2);
plot(lambda(375:2701),ffi_theta_lambda_massive(:,10),'LineWidth',2);
plot(lambda(375:2701),ffi_theta_lambda_massive(:,11),'LineWidth',2);
plot(lambda(375:2701),ffi_theta_lambda_massive(:,12),'LineWidth',2);
plot(lambda(375:2701),ffi_theta_lambda_massive(:,13),'LineWidth',2);
plot(lambda(375:2701),ffi_theta_lambda_massive(:,14),'LineWidth',2);
plot(lambda(375:2701),ffi_theta_lambda_massive(:,15),'LineWidth',2);
plot(lambda(375:2701),ffi_theta_lambda_massive(:,16),'LineWidth',2);
plot(lambda(375:2701),ffi_theta_lambda_massive(:,17),'LineWidth',2);
plot(lambda(375:2701),ffi_theta_lambda_massive(:,18),'LineWidth',2);
plot(lambda(375:2701),ffi_theta_lambda_massive(:,19),'LineWidth',2);
plot(lambda(375:2701),ffi_theta_lambda_massive(:,20),'LineWidth',2);
plot(lambda(375:2701),ffi_theta_lambda_massive(:,21),'LineWidth',2);
title('Type II phase matching for TH')
xlabel('\lambda (nm)', 'FontSize', 16);
ylabel('\theta (deg.)', 'FontSize', 16);
axis auto

%% 2w NOPA phase matching Type 1 ooe in BBO
omega=zeros(2701,1);
omega=(1./lambda).*100000000;
fi_theta_lambda_massive_2wnopa=zeros(2170,91);
wp=1/515*100000000;
d=100000;
for m=1:2701
    a=abs(omega(m)-wp);
    if a<d
        d=a;
        index_pump=m;
    end
```

```
end
for j=1:91
    for i=531:2701
        delta=10000000000000000;
        wi=wp-omega(i);
        d=1000000000000;
        index_k=1;
        index=1;
        for m=1:2701
            a=abs(omega(m)-wi);
            if a<d
                d=a;
                index=m;
            end
        end
        for k=j:91
            a=abs((wp*ne_t(index_pump,k-j+1))^2+(omega(i)*no(i)*cos(Fi(j)
                ))^2-2*wp*omega(i)*cos(Fi(j))*ne_t(index_pump,k-j+1)*no(i)
                -(wi*no(m))^2+(omega(i)*no(i)*sin(Fi(j)))^2)
            if a<delta
                delta=a;
                index_k=k;
            end
        end
        fi_theta_lambda_massive(i-374,j)=T(index_k)/2/pi*360; %%vylazit
            za predely
    end
end
figure(7);
plot(lambda(375:2701),fi_theta_lambda_massive(:,1));
hold on
plot(lambda(375:2701),fi_theta_lambda_massive(:,2),'LineWidth',2);
plot(lambda(375:2701),fi_theta_lambda_massive(:,3),'LineWidth',2);
plot(lambda(375:2701),fi_theta_lambda_massive(:,4),'LineWidth',2);
plot(lambda(375:2701),fi_theta_lambda_massive(:,5),'LineWidth',2);
plot(lambda(375:2701),fi_theta_lambda_massive(:,6),'LineWidth',2);
plot(lambda(375:2701),fi_theta_lambda_massive(:,7),'LineWidth',2);
plot(lambda(375:2701),fi_theta_lambda_massive(:,8),'LineWidth',2);
```

```
plot(lambda(375:2701),fi_theta_lambda_massive(:,9),'LineWidth',2);
plot(lambda(375:2701),fi_theta_lambda_massive(:,10),'LineWidth',2);
plot(lambda(375:2701),fi_theta_lambda_massive(:,11),'LineWidth',2);
plot(lambda(375:2701),fi_theta_lambda_massive(:,12),'LineWidth',2);
plot(lambda(375:2701),fi_theta_lambda_massive(:,13),'LineWidth',2);
plot(lambda(375:2701),fi_theta_lambda_massive(:,14),'LineWidth',2);
plot(lambda(375:2701),fi_theta_lambda_massive(:,15),'LineWidth',2);
plot(lambda(375:2701),fi_theta_lambda_massive(:,16),'LineWidth',2);
plot(lambda(375:2701),fi_theta_lambda_massive(:,17),'LineWidth',2);
plot(lambda(375:2701),fi_theta_lambda_massive(:,18),'LineWidth',2);
plot(lambda(375:2701),fi_theta_lambda_massive(:,19),'LineWidth',2);
plot(lambda(375:2701),fi_theta_lambda_massive(:,20),'LineWidth',2);
plot(lambda(375:2701),fi_theta_lambda_massive(:,21),'LineWidth',2);
title('Type II phase matching for TH')
xlabel('\lambda (nm)',  'FontSize', 16);
ylabel('\theta (deg.)', 'FontSize', 16);
axis auto
```